Draft version February 3, 2025
Typeset using LaTeX **twocolumn** style in AASTeX631

K-dwarf Radius Inflation and a 10-Gyr Spin-down Clock Unveiled through Asteroseismology of HD 219134 from the Keck Planet Finder

Yaguang Li (李亚光) [1] Daniel Huber [1] J. M. Joel Ong (王加冕) [1,*] Jennifer van Saders [1] R.R. Costa [2,3] Jens Reersted Larsen [4] Sarbani Basu [5] Timothy R. Bedding [6] Fei Dai (戴飞) [1] Ashley Chontos [7] Theron W. Carmichael [1] Daniel Hey [1] Hans Kjeldsen,[4] Marc Hon [8] Tiago L. Campante [2,3] Mário J. P. F. G. Monteiro [2,3] Mia Sloth Lundkvist [4] Nicholas Saunders [1,†] Howard Isaacson [9] Andrew W. Howard [10] Steven R. Gibson,[11] Samuel Halverson [12] Kodi Rider,[13] Arpita Roy [14] Ashley D. Baker [11] Jerry Edelstein [13] Chris Smith,[13] Benjamin J. Fulton [15] and Josh Walawender [16]

[1] *Institute for Astronomy, University of Hawai'i, 2680 Woodlawn Drive, Honolulu, HI 96822, USA*
[2] *Instituto de Astrofísica e Ciências do Espaço, Universidade do Porto, Rua das Estrelas, 4150-762 Porto, Portugal*
[3] *Departamento de Física e Astronomia, Faculdade de Ciências da Universidade do Porto, Rua do Campo Alegre, s/n, 4169-007 Porto, Portugal*
[4] *Stellar Astrophysics Centre (SAC), Department of Physics and Astronomy, Aarhus University, Ny Munkegade 120, 8000 Aarhus C, Denmark*
[5] *Department of Astronomy, Yale University, New Haven, CT 06511, USA*
[6] *Sydney Institute for Astronomy (SIfA), School of Physics, University of Sydney, NSW 2006, Australia*
[7] *Department of Astrophysical Sciences, Princeton University, 4 Ivy Lane, Princeton, NJ 08540, USA*
[8] *Kavli Institute for Astrophysics and Space Research, Massachusetts Institute of Technology, Cambridge, MA 02139, USA*
[9] *Department of Astronomy, 501 Campbell Hall, University of California, Berkeley, CA 94720, USA*
[10] *Department of Astronomy, California Institute of Technology, Pasadena, CA 91125, USA*
[11] *Caltech Optical Observatories, California Institute of Technology, Pasadena, CA 91125, USA*
[12] *Jet Propulsion Laboratory, California Institute of Technology, 4800 Oak Grove Drive, Pasadena, CA 91109, USA*
[13] *Space Sciences Laboratory, University of California, Berkeley, CA 94720, USA*
[14] *Astrophysics & Space Institute, Schmidt Sciences, New York, NY 10011, USA*
[15] *NASA Exoplanet Science Institute/Caltech-IPAC, California Institute of Technology, Pasadena, CA 91125, USA*
[16] *W. M. Keck Observatory, 65-1120 Mamalahoa Hwy, Kamuela, HI 96743, USA*

ABSTRACT

We present the first asteroseismic analysis of the K3 V planet host HD 219134, based on four consecutive nights of radial velocities collected with the Keck Planet Finder. We applied Gold deconvolution to the power spectrum to disentangle modes from sidelobes in the spectral window, and extracted 25 mode frequencies with spherical degrees $0 \leq \ell \leq 3$. We derive the fundamental properties using five different evolutionary-modeling pipelines and report a mass of 0.763 ± 0.020 (stat) ± 0.007 (sys) $M_\odot$, a radius of 0.748 ± 0.007 (stat) ± 0.002 (sys) $R_\odot$, and an age of 10.151 ± 1.520 (stat) ± 0.810 (sys) Gyr. Compared to the interferometric radius 0.783 ± 0.005 $R_\odot$, the asteroseismic radius is 4% smaller at the 4-σ level — a discrepancy not easily explained by known interferometric systematics, modeling assumptions on atmospheric boundary conditions and mixing lengths, magnetic fields, or tidal heating. HD 219134 is the first main-sequence star cooler than 5000 K with an asteroseismic age estimate and will serve as a critical calibration point for stellar spin-down relations. We show that existing calibrated prescriptions for angular momentum loss, incorporating weakened magnetic braking with asteroseismically constrained stellar parameters, accurately reproduce the observed rotation period. Additionally, we revised the masses and radii of the super-Earths in the system, which support their having Earth-like compositions. Finally, we confirm that the oscillation amplitude in radial velocity scales as $(L/M)^{1.5}$ in K dwarfs, in contrast to the $(L/M)^{0.7}$ relation observed in G dwarfs. These findings provide significant insights into the structure and angular momentum loss of K-type stars.

yaguangl@hawaii.edu

Keywords: Stellar scillations — Stellar rotation — K dwarf stars

1. INTRODUCTION

Asteroseismology, the study of stellar oscillations, is a powerful method for measuring fundamental stellar properties and studying interior dynamics. Early detections of oscillations in solar-type stars—see T. R. Bedding & H. Kjeldsen (2003) for a review—were made possible through ground-based radial velocity (RV) observations, such as those observed in Procyon (T. M. Brown et al. 1991; B. Mosser et al. 1998; M. Martić et al. 1999), β Hyi (T. R. Bedding et al. 2001) and α Cen A (F. Bouchy & F. Carrier 2001, 2002). These observations confirmed the presence of solar-like oscillations in cool stars beyond the Sun, which are stochastically excited and damped by surface turbulence (P. Goldreich & D. A. Keeley 1977).

In stars with solar-like oscillations, acoustic modes are observed around the frequency of maximum power, $\nu_{\rm max}$. Their non-rotating frequencies are well approximated by the asymptotic relation involving two quantum numbers, the radial order, n, and angular degree, ℓ (M. Tassoul 1980; P. H. Scherrer et al. 1983):

$$\nu_{n,\ell} \simeq \Delta\nu \left(n + \frac{\ell}{2} + \epsilon \right) - \delta\nu_{0,\ell}. \quad (1)$$

The large frequency separation, $\Delta\nu$, depends primarily on the sound travel time across the star and, to first order, scales with the square root of the mean stellar density (R. K. Ulrich 1986). The phase offset, ϵ, generally falls between 0.8 and 1.6 in main-sequence stars (T. R. White et al. 2012), and depends on the physical structure of the star, primarily as concentrated near the center and surface (I. W. Roxburgh & S. V. Vorontsov 2003). The small separation, $\delta\nu_{0,\ell}$ quantifies the frequency offsets between modes of different ℓ but with same n. In main-sequence stars, it is sensitive to the chemical gradient near the core (M. Tassoul 1990; I. W. Roxburgh & S. V. Vorontsov 1994), making it a useful diagnostic for tracing hydrogen-burning processes and, therefore, for determining stellar ages on the main sequence (J. Christensen-Dalsgaard 1984; T. R. White et al. 2011; M. Hon et al. 2024a).

Since the advent of space missions in the 2000s, photometric measurements have become a primary method for detecting stellar oscillations, with the significant advantage of allowing simultaneous observations of many stars. Missions like WIRE (P. Hacking et al. 1997), MOST (J. M. Matthews et al. 2000), CoRoT (M. Auvergne et al. 2009), Kepler (W. J. Borucki et al. 2010) and TESS (G. R. Ricker et al. 2015) have substantially increased the number of detections of solar-like oscillations in G- and F-type main-sequence stars, as well as in sub- and red giants spanning a wide range of evolutionary stages (see reviews by W. J. Chaplin & A. Miglio 2013; J. Jackiewicz 2021). The high precision of these photometric observations allows for detailed analysis of oscillation modes, probing the structure and dynamics of stellar interiors, including rotation, magnetism, and binary merging (see C. Aerts 2021, for a review).

Recent significant advances in Doppler precision, driven by the search for Earth-like planets, have opened new opportunities for detecting stellar oscillations with much lower amplitudes. Extreme Precision Radial Velocity (EPRV) techniques now achieve radial velocity measurements with precisions in the range of 10–30 cm/s (D. A. Fischer et al. 2016; J. T. Wright 2018). This level of precision makes it possible to detect the intrinsic oscillations of K dwarfs, which have amplitudes ranging from 1 to 6 cm/s. These oscillations are very challenging to detect in photometry due to the presence of granulation noise, which is significantly lower (relative to the oscillations) in RV measurements from spatially-averaged line profiles (J. W. Harvey 1988; F. Grundahl et al. 2007; M. Asplund et al. 2000; H. Kjeldsen & T. R. Bedding 2011).

Until recently, the only K dwarf with oscillations detected in RV was the bright K1 V star α Cen B (F. Carrier & G. Bourban 2003; H. Kjeldsen et al. 2005). The arrival of EPRV instruments has however now ushered in a new era of K-dwarf asteroseismology Oscillations in the K5 V star ϵ Indi were reported by T. L. Campante et al. (2024) with six half-nights of observations with ESPRESSO on the VLT (F. Pepe et al. 2021), and also at lower signal-to-noise with HARPS and UVES by M. S. Lundkvist et al. (2024). M. Hon et al. (2024b) detected oscillations in the K0 V star σ Draconis using one night of observations with the Keck Planet Finder (KPF) on the Keck I telescope (S. R. Gibson 2016; S. R. Gibson et al. 2018, 2020, 2024). Although TESS photometryalso shows oscillations in σ Draconis from 14 sectors of data, the KPF RV power spectrum revealed oscillation modes over a broader frequency range due to the higher signal-to-noise ratio achieved in the RV data. Figure 1 illustrates the expanding asteroseismol-

* NASA Hubble Fellow
† NSF Graduate Research Fellow

ogy footprint, with EPRV techniques populating the K dwarf parameter space.

While a single night of data is sufficient to detect both $\nu_{\rm max}$ and $\Delta\nu$ (assuming SNR is reached), achieving the resolution required to measure small frequency spacings like $\delta\nu_{0,l}$ remains challenging. For example, an 8-hour time series only provides a frequency resolution of ≈34 μHz, which exceeds the typical $\delta\nu_{0,2}$ values of about 10 μHz for main-sequence stars (e.g. T. R. White et al. 2011). We can address this limitation using multiple nights of data. For this paper, we have obtained four nights of data collected with the KPF, corresponding to a frequency resolution of ≈3 μHz. We report both the detection of oscillations in HD 219134 and the determination of its benchmark mass, radius, and age via asteroseismology.

1.1. *The K3 V exoplanet host HD 219134*

HD 219134 (HR 8832) is a nearby K3 V dwarf (d = 6.5 pc; $V = 5.57$). It has an angular diameter precisely measured through interferometry (R. Ligi et al. 2019; D. Huber 2016; A. Elliot et al. 2025), enabling an accurate determination of its radius (see §3.1). Asteroseismology provides an independent method to estimate the stellar radius by probing the star's interior through oscillation frequencies. This star presents an opportunity to directly compare these two techniques.

HD 219134 has a rotation period of ≈42 days (F. Motalebi et al. 2015; C. P. Folsom et al. 2018). Cool stars experience gradual spin-down over time, making rotation period a valuable proxy for stellar age — a principle underpinning gyrochronology. However, the applicability of the rotation-age relation relies on calibrations using stars with well-known ages, primarily those in open clusters (J. L. Curtis et al. 2020). HD 219134 rotates more slowly than all stars of similar spectral type in the current open cluster calibrators. Furthermore, recent studies of K-dwarf stars have revealed a phase of apparently stalled spin-down (J. L. Curtis et al. 2019, 2020; M. A. Agüeros et al. 2018). It remains unclear for how long the epoch of stalling persists or the degree to which it affects the rotation rates of old stars. Measuring the age of this star using asteroseismology provides a valuable test of the rotation-age spin-down relationship for stars at advanced ages.

HD 219134 hosts five known RV planets, including the transiting super-Earths HD 219134 b and c, whose orbital periods are 3.09 and 6.87 days (S. S. Vogt et al. 2015; F. Motalebi et al. 2015; S. Seager et al. 2021; L. J. Rosenthal et al. 2021; M. Gillon et al. 2017; A. Kokori et al. 2023). A detailed seismic characterization of the host star's mass and radius refines the properties of these planets.

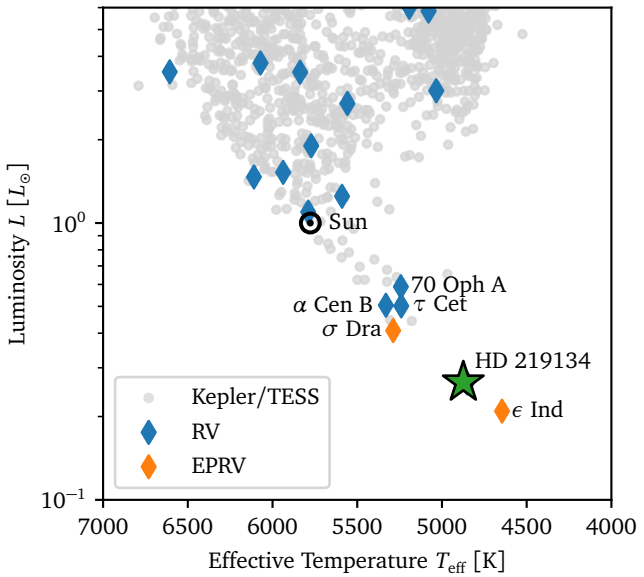

Figure 1. H–R diagram showing the footprint of asteroseismology conducted using space-based photometry (e.g. W. J. Chaplin et al. 2015; M. N. Lund et al. 2016, 2017; A. Serenelli et al. 2017; J. Yu et al. 2018; Y. Li et al. 2020; E. Hatt et al. 2023; L. González-Cuesta et al. 2023; J. Zhou et al. 2024; M. N. Lund et al. 2024) and ground-based radial velocity (RV) measurements (e.g. H. Kjeldsen et al. 2005; F. Carrier & P. Eggenberger 2006; T. C. Teixeira et al. 2009). The diagram highlights recent contributions made possible by Extreme Precision Radial Velocity (EPRV) instruments (T. L. Campante et al. 2024; M. Hon et al. 2024b), which have significantly expanded the parameter space for K dwarf studies.

The paper is organized as follows. We report our detection of oscillations and extract oscillation frequencies (§2). We derive stellar properties using asteroseismic modeling (§3). We highlight the discrepancy between our asteroseismic radius and an interferometric radius and explore potential explanations (§4). We discuss the implication of stellar age for gyrochronology by testing models with angular momentum loss (§5). We revise planet properties using the new stellar mass and radius (§6). Finally, we analyze mode amplitudes (§7), and present our conclusions (§8).

2. OSCILLATION FREQUENCIES

We obtained approximately 9 hours of observations per night over 4 consecutive nights, from September 25 to 28, 2024 (HST), using the Keck Planet Finder (KPF) on the Keck I telescope (S. R. Gibson 2016; S. R. Gibson et al. 2018, 2020, 2024). A total of 2,155 radial velocity measurements were collected. We used 45-second exposures, with a readout time of 15 seconds, resulting in

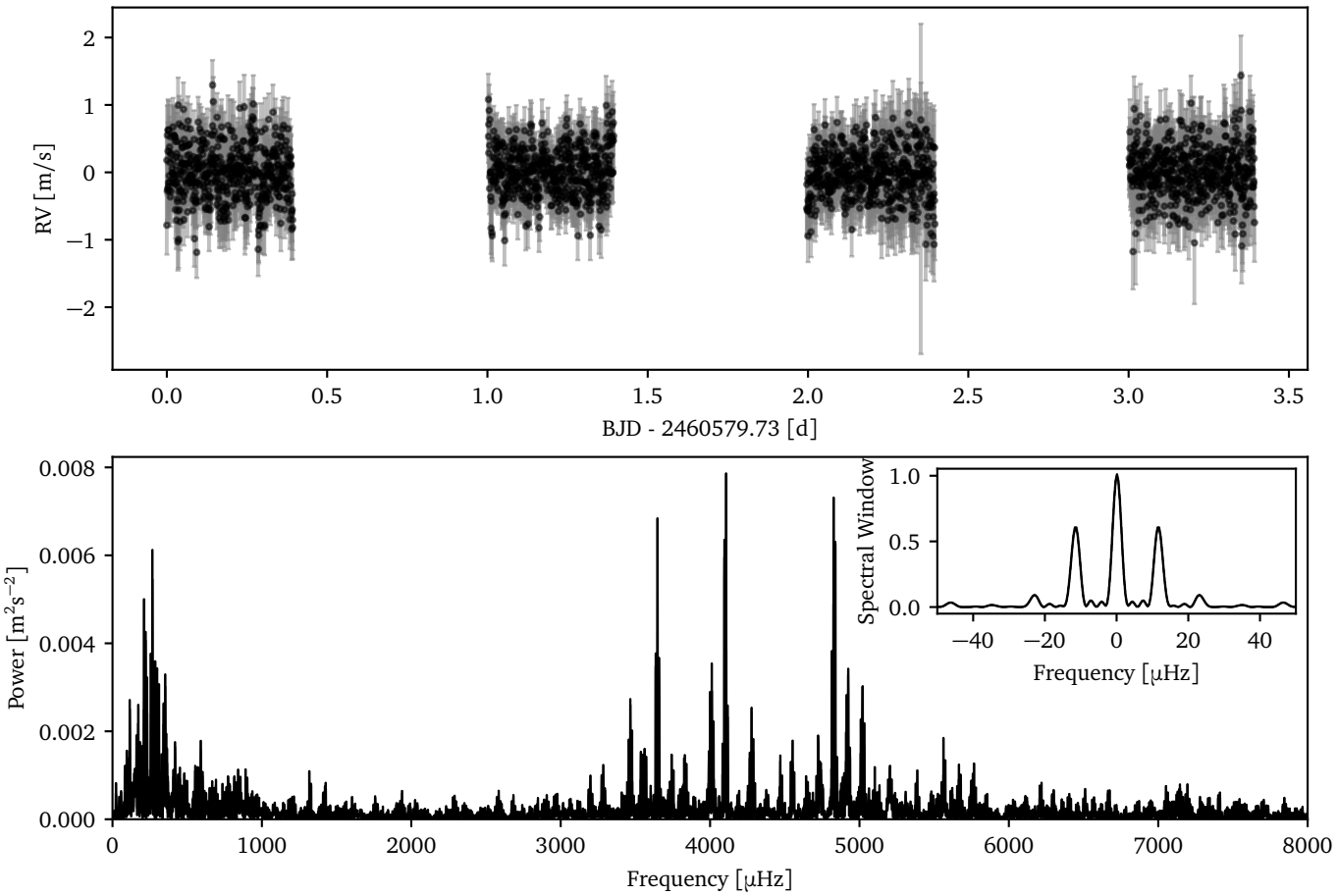

Figure 2. Asteroseismic observations of HD 219134 over four consecutive nights using the Keck Planet Finder. Top: Radial-velocity time series after filtering out signals with periods longer than 1.2 hours. Bottom: Power spectrum of the RV time series, weighted by the reported RV uncertainties, displaying a clear power excess around 4500 μHz. The inset shows the spectral window.

a cadence of 1 minute per observation. Observing conditions were excellent and stable, with seeing ranging from 0.4" to 0.8". The signal-to-noise ratio (SNR) of the spectra at 747 nm remained consistently around 500.

The spectra were processed with KPF Data Reduction Pipeline (DRP; S. R. Gibson et al. 2020)[1]. KPF DRP executes several processing steps, including quadrant stitching, flat-field correction, order tracing, optimal spectral extraction, and wavelength calibration. RVs are determined from a cross-correlation function (CCF) mask method, using the same K2 binary CCF mask as in the ESPRESSO pipeline (F. Pepe et al. 2021). A mean position of the CCF is fitted using a Gaussian plus top-hat function. RVs are computed separately for each of the three KPF slices and for each camera (green and red). The RVs from individual slices are combined through a weighted average, where the weights are inversely proportional to the photon-limited RV uncertainties for each slice. The RVs from the cameras are adjusted by median subtraction and corrected for instrumental drift, based on laser frequency comb spectra obtained before and after the stellar RV observations. The drift-corrected RV time series for the two cameras are then combined into a single dataset using a flux-weighted mean.

To calculate the power spectrum of the RV time series, we applied the Lomb-Scargle method, using the reported RV uncertainties as weights (N. R. Lomb 1976; J. D. Scargle 1982). Normalization of the power spectrum followed the convention of H. Kjeldsen & T. R. Bedding (1995): a sine wave with amplitude A produces a peak with a height of A^2 in the power spectrum, and $A^2 T_{\rm obs}$ in the power density spectrum, with $T_{\rm obs}$ being the effective observing duration. In Figure 2, we show the RV time series, along with the power spectrum.

Given that the power spectrum in the high-frequency regime contains only white noise, from it we estimate

[1] https://github.com/Keck-DataReductionPipelines/KPF-Pipeline?tab=readme-ov-file

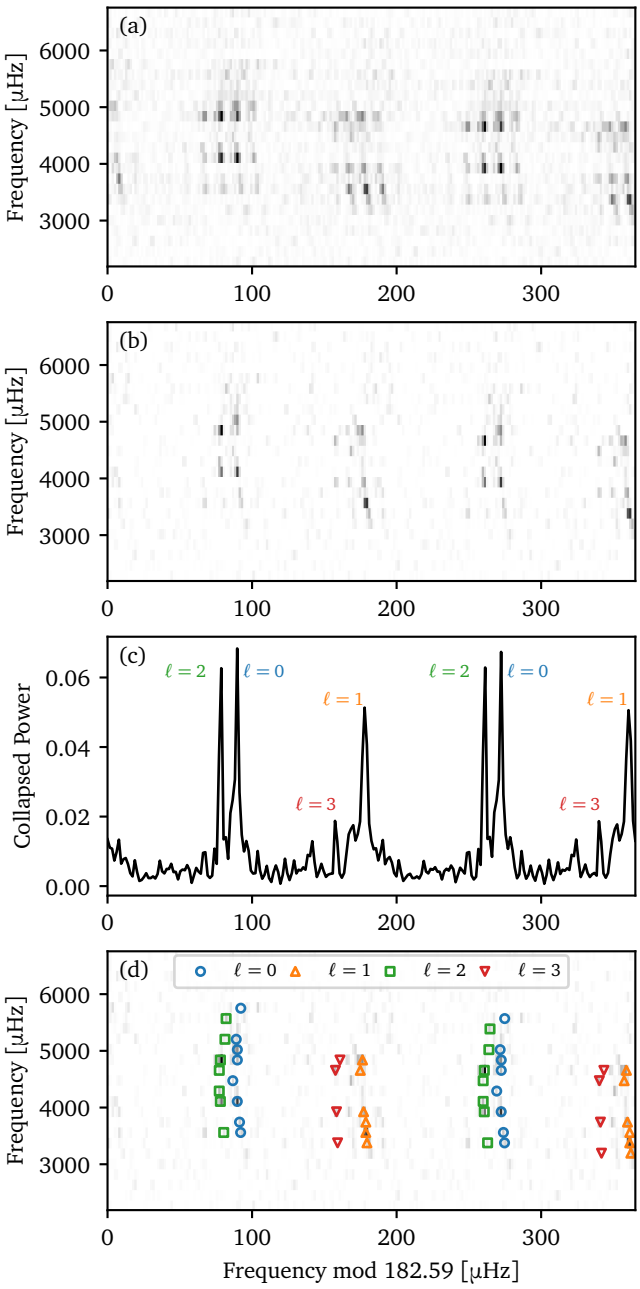

Figure 3. Échelle diagrams showing structures of regular frequency spacings. Panel a: replicated échelle diagram of the original power spectrum. Panel b: échelle diagram of the power spectrum, deconvolved from the spectral window and then convolved with a 1 μHz width Gaussian filter for clarity. Panel c: collapsed échelle diagram, summing the power along the y-axis of panel b. Panel d: same as panel b, but highlighting the extracted oscillation modes.

the time-domain RV scatter, $\sigma_{\rm noise}$, due to photon and instrumental noise. The scatter is calculated as $\sigma_{\rm noise} = \sqrt{P_{\rm mean}/(2\Delta t)}$, where $P_{\rm mean}$ is the mean power density between 6500 μHz and 8000 μHz, and Δt is the cadence. We obtained a value of time-domain scatter at 0.37 m/s, which is in agreement with the average RV uncertainties reported from the reduction pipeline at 0.41 m/s.

Table 1. Oscillation frequencies of HD 219134, including corrections for line-of-sights Doppler shifts.

n	l	$\nu_{n,\ell}$ [μHz]	$\sigma(\nu_{n,\ell})$ [μHz]
18	0	3561.03	0.58
19	0	3742.84	1.07
21	0	4106.45	0.64
23	0	4468.50	0.91
25	0	4836.80	0.95
26	0	5019.39	0.85
27	0	5201.19	0.95
30	0	5752.07	1.03
17	1	3465.84	0.84
18	1	3647.65	0.43
19	1	3830.23	0.90
20	1	4011.26	0.65
24	1	4739.26	0.95
25	1	4923.41	0.64
17	2	3549.33	0.62
20	2	4094.75	0.85
21	2	4276.55	1.05
23	2	4641.73	1.00
24	2	4825.09	0.52
26	2	5193.39	1.12
28	2	5559.34	0.98
16	3	3445.55	1.05
19	3	3992.53	1.07
23	3	4722.10	0.93
24	3	4907.80	1.02

Regular data gaps in time domain inevitably cause multiple peaks near the true frequency in frequency domain, a phenomenon known as spectral leakage. The observed power spectrum is the convolution of the true spectrum (as in continuous and infinite time series) against the spectral window function. To examine the shape of the spectral window for our dataset, we generate sine and cosine waves at an arbitrary test frequency, sampled at the timestamps of our RV data. We then calculate and average the power spectra of both waves, which helps reduce edge effects from signal apodization. The inset of Figure 2 shows the spectral window centred around the test frequency. The strongest sidelobes appear at multiples of 1 c/d (≈11.57 μHz), due to the existence of daily gaps.

This presents a significant challenge in identifying the $\delta\nu_{02}$ spacing, as it is very close to 1 c/d in K-type main-sequence stars (T. R. White et al. 2011). This can be

seen from Figure 3(a), which shows the power spectrum folded into segments of $\Delta\nu$ and displayed in an échelle format. In such diagrams, modes of the same spherical degree ℓ form vertical ridges from consecutive radial orders n, as predicted by the asymptotic relation (Equation 1). Based on theoretical predictions of the phase offset ϵ (T. R. White et al. 2011; J. M. J. Ong & S. Basu 2019), we expect ϵ to be approximately 1.4 given the $\Delta\nu$ value of HD 219134. This implies that the ridges in Figure 3(a) at an abscissa of ≈90 μHz corresponds to the $\ell = 0$ and $\ell = 2$ modes, while the ridge at 180 μHz corresponds to the $\ell = 1$ (and $\ell = 3$, if present) modes. Due to geometric cancellation, only oscillation modes with low spherical degrees (ℓ=0–3) are expected to be visible. However, Figure 3(a) shows more than four vertical ridges, many of which are sidelobes — replicas of true ridges appearing at multiples of 1 c/d. In particular, the true $\ell = 2$ ridge could overlap with the left sidelobe of the $\ell = 0$ ridge, due to the proximity of $\delta\nu_{02}$ to 1 c/d.

To better reveal the frequency structure, we deconvolved the power spectrum against the spectral window using the Gold algorithm (R. Gold 1964), and in particular applying the numerical implementation of it described by M. Morháč et al. (2003). The algorithm takes the power spectrum and the spectral window as inputs, and iteratively solves for the underlying true spectrum with some regularization[2]. We selected this algorithm over other deconvolution schemes for its desirable properties: (1) it ensures the solution remains positive when both the input data and spectral window are positive; and (2) it provides non-oscillating solutions for isolated peaks, effectively suppressing ringing artifacts (M. Morháč & V. Matoušek 2009). A quantitative evaluation of its performance in asteroseismic applications will be presented in a forthcoming paper; in this work, we apply it solely as a visual aid to mode identification, but otherwise apply traditional fitting techniques to derive estimates and uncertainties of mode frequencies. Figure 3(b) shows the spectrum after deconvolution, revealing clear $\ell = 0$–3 mode ridges. This is more apparent in Figure 3(c), which shows the collapsed power spectrum from summing power along the vertical direction in Figure 3(b).

From Figure 3(b) and (c), we can identify the peaks along each ridge, which we preliminarily consider as candidate oscillation modes. We extracted their frequencies by simultaneously fitting sine waves at these frequencies to the RV time series, obtaining the corresponding amplitudes and phases. Signals with amplitudes exceeding 3.5 times the noise level (0.37 m/s) are retained as the final list of modes. These are highlighted in Figure 3(d).

Furthermore, we corrected the line-of-sight Doppler shifts for these frequencies following G. R. Davies et al. (2014), using a radial velocity of −18368 m/s based on an average value over four nights. This adjustment reduced the frequencies by an average of ≈0.27 μHz.

Frequency uncertainties were calculated using the method described by H. Kjeldsen & T. R. Bedding (2012):

$$\sigma(\nu) \approx 0.44\sqrt{\pi/N}\sigma_{\rm noise}a^{-1}\sqrt{T_{\rm obs}^{-2}+\tau^{-2}}, \qquad (2)$$

where N is the number of points in the time series, a is the mode amplitude, and τ is the mode lifetime. For the Sun, the mode lifetime is typically 1–3 days (W. J. Chaplin et al. 2000; T. R. Bedding et al. 2004), and it increases for cooler stars. We assumed a conservative mode lifetime of 3 days for this star in the uncertainty calculation.

Table 1 lists the determined oscillation frequencies. Furthermore, we fitted Equation 1 to these frequencies and obtained the following asymptotic parameters: $\Delta\nu = 182.799 \pm 0.069$ μHz, $\epsilon = 1.455 \pm 0.010$, $\delta\nu_{01} = 3.81 \pm 0.41$ μHz, $\delta\nu_{02} = 10.90 \pm 0.41$ μHz, and $\delta\nu_{03} = 22.27 \pm 0.59$ μHz.

3. ASTEROSEISMIC MODELING

In this section, we derive the stellar parameters of HD 219134 using modern asteroseismic modeling techniques. We first describe the input observables used in the modeling process (§3.1), followed by an overview of the modeling methodology and key assumptions (§3.2). Finally, we provide brief comments on the derived stellar age and its implications (§3.3).

3.1. *Classical Constraints*

To derive a bolometric flux for HD 219134 we use optical broadband photometry from *Tycho* (E. Høg et al. 2000) since near-infrared 2MASS photometry is saturated and systematic errors for bright stars are not yet well calibrated in Gaia (M. Riello et al. 2021). The star has a $B_{\rm T}$ magnitude of 6.861 ± 0.015 and a $V_{\rm T}$ magnitude of 5.674 ± 0.009. Incorporating the Gaia DR3 distance and bolometric corrections, we used `ISOCLASSIFY` (D. Huber et al. 2017; T. A. Berger et al. 2020) to calculate bolometric fluxes of $f_{\rm bol} = (1.881 \pm 0.055) \times 10^{-7}$ erg s^{-1} cm^{-2} and $f_{\rm bol} = (1.981 \pm 0.054) \times 10^{-7}$ erg s^{-1} cm^{-2}, based on $B_{\rm T}$ and $V_{\rm T}$, respectively. R. Ligi et al. (2019) determined the bolometric flux by fitting its spectral energy distribution, finding $f_{\rm bol} = (1.986 \pm 0.024) \times 10^{-7}$ erg s^{-1} cm^{-2}. Due to the higher precision of the $V_{\rm T}$ magnitude, we adopted its corresponding bolometric

[2] https://github.com/parallelpro/maemae

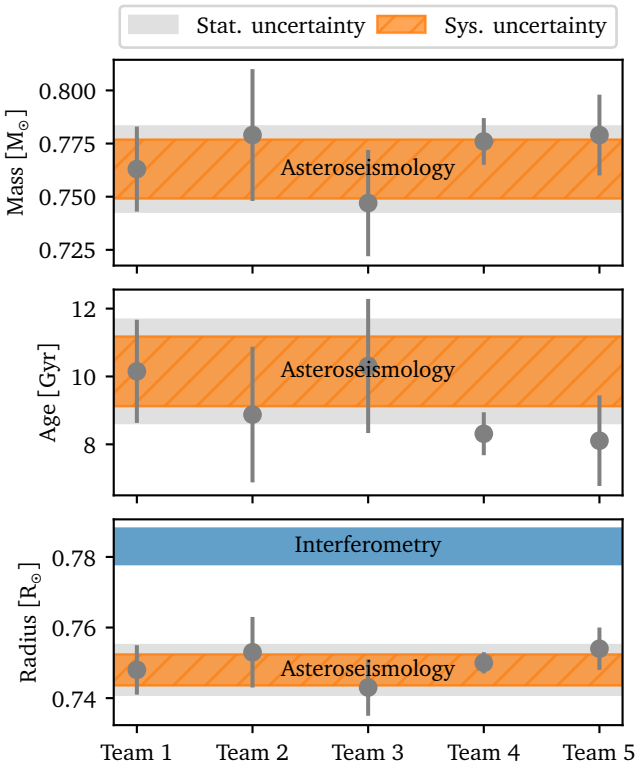

Figure 4. Stellar mass, radius and age derived from five independent asteroseismic modeling teams. The asteroseismic radius is compared against the interferometric radius based on an angular diameter measurement from A. Elliot et al. (2025).

flux value. To refine the uncertainty, we calculated the standard deviation of all three flux measurements to account for systematic uncertainties, and combined this in quadrature with the original uncertainty. This yields a final value of $f_{\rm bol} = (1.981 \pm 0.072) \times 10^{-7}$ erg s^{-1} cm^{-2}.

The star's angular diameter was measured using CHARA/VEGA by R. Ligi et al. (2019) as $\theta = 1.035 \pm 0.021$ mas. Combined with the Gaia DR3 distance of $D = 6.541 \pm 0.002$ pc (C. A. L. Bailer-Jones et al. 2021a), this results in a stellar radius of $R = 0.728 \pm 0.015$ R$_\odot$ via

$$R = \frac{1}{2}\theta D. \tag{3}$$

We calculated the star's interferometric effective temperature based on the bolometric flux and angular diameter:

$$T_{\rm eff} = 4^{1/4} f_{\rm bol}^{1/4} \sigma_{\rm SB}^{-1/4} \theta^{-1/2}, \tag{4}$$

where $\sigma_{\rm SB}$ is the Stefan-Boltzmann constant. The result is $T_{\rm eff} = 4854 \pm 66$ K, consistent with the spectroscopic temperature measured by L. J. Rosenthal et al. (2021), who reported $T_{\rm eff} = 4817 \pm 62$ K. The measured metallicity from L. J. Rosenthal et al. (2021) is [Fe/H] $= 0.083 \pm 0.058$ dex.

An alternative solution for the star's angular diameter, provided by A. Elliot et al. (2025), is $\theta = 1.114 \pm 0.007$ mas, which corresponds to a stellar radius of $R_\star = 0.783 \pm 0.015$ R$_\odot$, and an interferometric temperature of $T_{\rm eff} = 4678 \pm 45$ K. In principle, this angular diameter should be more accurate, given that the measurement spans a wider range of spatial frequencies. However, asteroseismic modeling using this interferometric $T_{\rm eff}$ predicts a radius that differs from the interferometric radius by $> 3\sigma$. This suggests the two methods may not be strictly compatible, resulting from either unaccounted interferometric systematics or inaccuracies in the stellar models (see §4 for detail).

To maximise compatibility between inputs and stellar models, we adopted a conservative set of input observables for modeling: the interferometric $T_{\rm eff}$ based on R. Ligi et al. (2019), spectroscopic [Fe/H] from L. J. Rosenthal et al. (2021), and the oscillation frequencies presented in Table 1. We deliberately excluded the bolometric flux and radius as direct constraints, despite their high precision, to avoid potential inconsistencies between these values and the asteroseismic constraints. We summarize the stellar properties in Table 3.

3.2. *Frequency modeling*

For frequency modeling, we employed five distinct modeling pipelines to assess the systematic uncertainties arising from different choices of input physics and the use of various codes.

Stellar evolution codes used by the five teams include MESA (B. Paxton et al. 2011, 2013, 2015, 2018, 2019; A. S. Jermyn et al. 2023; N. Moedas et al. 2024), GARSTEC (A. Weiss & H. Schlattl 2008), and YREC (P. Demarque et al. 2008). Pulsation codes used for calculating oscillation frequencies include GYRE (R. H. D. Townsend & S. A. Teitler 2013), ADIPLS (J. Christensen-Dalsgaard 2008), and H. M. Antia & S. Basu (1994).

The input physics used by the five teams also differ. Treatments of atmospheric boundary conditions include the Eddington (A. S. Eddington 1926) and Krishna-Swamy (K. S. Krishna Swamy 1966) T-τ relations, and pre-computed photosphere tables (P. H. Hauschildt et al. 1999a,b; F. Castelli & R. L. Kurucz 2003; R. Trampedach et al. 2014). Choices of nuclear reaction rates vary from R. H. Cyburt et al. (2010), C. Angulo et al. (1999), A. Formicola et al. (2004), J. W. Hammer et al. (2005), and E. G. Adelberger et al. (1998).

Table 2. Summary of the frequency modeling.

	Team 1	Team 2	Team 3	Team 4	Team 5
Model Configuration					
Stellar evolution code	MESA r240301	MESA r12778	GARSTEC v2015	YREC	GARSTEC v2020
Pulsation code	GYRE v7.1	GYRE v5	ADIPLS v0.4	H. M. Antia & S. Basu (1994)	GYRE v7.2
Opacities & EOS	OPAL	OPAL	OPAL	OPAL	OPAL
Atmospheric boundary condition	P. H. Hauschildt et al. (1999a,b) F. Castelli & R. L. Kurucz (2003)	K. S. Krishna Swamy (1966)	A. S. Eddington (1926)	A. S. Eddington (1926)	R. Trampedach et al. (2014)
Metal mixture	M. Asplund et al. (2009)	M. Asplund et al. (2009)	M. Asplund et al. (2009)	N. Grevesse & A. J. Sauval (1998)	N. Grevesse & A. J. Sauval (1998)
Nuclear reaction rate	R. H. Cyburt et al. (2010) C. Angulo et al. (1999)	R. H. Cyburt et al. (2010) C. Angulo et al. (1999)	C. Angulo et al. (1999) A. Formicola et al. (2004) J. W. Hammer et al. (2005)	E. G. Adelberger et al. (1998) A. Formicola et al. (2004)	C. Angulo et al. (1999) A. Formicola et al. (2004) J. W. Hammer et al. (2005)
Mixing length formulation	L. Henyey et al. (1965)	J. P. Cox & R. T. Giuli (1968)	E. Böhm-Vitense (1958)	E. Böhm-Vitense (1958)	J. P. Cox & R. T. Giuli (1968)
Mixing length parameter $\alpha_{\rm MLT}$	Free	Solar-calibrated	Free	Free	Varying vs. solar-calibrated
$\alpha_{\rm MLT,\odot}$	1.96	1.71	1.79	1.84	1.83
Convective overshoot	F. Herwig (2000) $f_{\rm ov,shell} = 0.0174$	None	None	None	None
Extra-mixing	None	Gravitational settling Turbulent mixing	A. A. Thoul et al. (1994)	A. A. Thoul et al. (1994)	A. A. Thoul et al. (1994) Diffusive mixing
Surface correction	W. H. Ball & L. Gizon (2014) two-term +Y. Li et al. (2023) ensemble correction	T. Sonoi et al. (2015)	W. H. Ball & L. Gizon (2014) cubic-term	W. H. Ball & L. Gizon (2014) two-term	W. H. Ball & L. Gizon (2014) two-term + I. W. Roxburgh (2016) ϵ-matching
Grid free parameters	M, [M/H], $\alpha_{\rm MLT}$, $Y_{\rm init}$	M, [M/H], $Y_{\rm init}$	M, [M/H], $\alpha_{\rm MLT}$, $Y_{\rm init}$	M, [M/H], $\alpha_{\rm MLT}$, $Y_{\rm init}$	M, [M/H], $Y_{\rm init}$
Derived Stellar Parameters					
Mass $M_\star$ [$M_\odot$]	0.763 ± 0.020	0.779 ± 0.031	0.773 ± 0.038	0.776 ± 0.011	0.779 ± 0.019
Radius $R_\star$ [$R_\odot$]	0.748 ± 0.007	0.753 ± 0.010	0.751 ± 0.012	0.750 ± 0.003	0.754 ± 0.006
Age $t_\star$ [Gyr]	10.2 ± 1.5	8.9 ± 2.0	9.2 ± 2.5	8.3 ± 0.6	8.1 ± 1.3
Density $\rho_\star$ [$\rho_\odot$]	1.823 ± 0.003	1.825 ± 0.001	1.826 ± 0.100	1.824 ± 0.001	1.818 ± 0.007
Surface gravity $\log g_\star$ [dex]	4.577 ± 0.001	4.576 ± 0.006	4.570 ± 0.005	4.575 ± 0.002	4.575 ± 0.004
$Y_{\rm init}$	0.270 ± 0.023	0.278 ± 0.022	0.279 ± 0.019	0.280 ± 0.005	0.272 ± 0.010
$\alpha_{\rm MLT}/\alpha_{\rm MLT,\odot}$	0.95 ± 0.05	—	1.03 ± 0.07	0.94 ± 0.04	—

Table 3. Star and planet properties.

Property	Value	Reference
HD 219134		
Photometry		
B_T-band magnitude	6.861 ± 0.015	E. Høg et al. (2000)
V_T-band magnitude	5.674 ± 0.009	E. Høg et al. (2000)
Bolometric flux $f_{\rm bol}$ [erg s^{-1} cm^{-2}]	(1.981 ± 0.072) $\times 10^{-7}$	This work
Astrometry		
Distance [pc]	6.5409 ± 0.0023	C. A. L. Bailer-Jones et al. (2021b)
Luminosity $L_\star$ [L$_\odot$]	0.265 ± 0.011	§3.1
Interferometry		
Angular diameter θ [mas]	1.035 ± 0.021	R. Ligi et al. (2019)
Effective temperature $T_{\rm eff}$ [K]	4854 ± 66 [1]	§3.1
Radius $R_\star$ [R$_\odot$]	0.728 ± 0.015	§3.1
Angular diameter θ [mas]	1.114 ± 0.007	A. Elliot et al. (2025)
Effective temperature $T_{\rm eff}$ [K]	4678 ± 45	§3.1
Radius $R_\star$ [R$_\odot$]	0.783 ± 0.005	§3.1
Spectroscopy		
Effective temperature $T_{\rm eff}$ [K]	4817 ± 62	L. J. Rosenthal et al. (2021)
Metallicity [Fe/H] [dex]	0.08 ± 0.06 [1]	L. J. Rosenthal et al. (2021)
Asteroseismology		
$\Delta\nu$ [μHz]	182.799 ± 0.069	§2
ϵ	1.455 ± 0.010	§2
$\delta\nu_{01}$ [μHz]	3.81 ± 0.41	§2
$\delta\nu_{02}$ [μHz]	10.90 ± 0.41	§2
$\delta\nu_{03}$ [μHz]	22.27 ± 0.59	§2
$\nu_{\rm max}$ [μHz]	4651 ± 301	§7
$A_{\rm osc}$ [cm s^{-1}]	4.23 ± 0.41	§7
Mass $M_\star$ [M$_\odot$]	0.763 ± 0.020 (stat) ± 0.014 (sys)	§3.2
Radius $R_\star$ [R$_\odot$]	0.748 ± 0.007 (stat) ± 0.004 (sys)	§3.2
Age $t_\star$ [Gyr]	10.2 ± 1.5 (stat) ± 1.0 (sys)	§3.2
Density $\rho_\star$ [$\rho_\odot$]	1.823 ± 0.003 (stat) ± 0.003 (sys)	§3.2
Surface gravity $\log g_\star$ [dex]	4.577 ± 0.001 (stat) ± 0.003 (sys)	§3.2
Initial helium abundance $Y_{\rm init}$	0.27 ± 0.02 (stat) ± 0.01 (sys)	§3.2
Rotation		
Rotation period $P_{\rm rot}$ [d]	41 ± 2.4	§5.1
HD 219134b		
Mass [M$_\oplus$]	4.59 ± 0.16	§6
Radius [R$_\oplus$]	1.542 ± 0.054	§6
HD 219134c		
Mass [M$_\oplus$]	4.23 ± 0.20	§6
Radius [R$_\oplus$]	1.455 ± 0.046	§6

NOTE—1. Used for asteroseismic modeling.

The mixing length formulations include L. Henyey et al. (1965), J. P. Cox & R. T. Giuli (1968) and E. Böhm-Vitense (1958), with some teams using solar-calibrated mixing length parameters, others treating it as a free variable, and still others using calibrated prescriptions for varying it. Different teams employed different correction procedures for near-surface modeling errors (which we discuss in more depth in §4.2): the empirical correction formulae (W. H. Ball & L. Gizon 2014) and the nonparametric ϵ-matching technique (I. W. Roxburgh 2016), potentially with additional calibrations against 3D models (T. Sonoi et al. 2015) or from an empirical ensemble (Y. Li et al. 2023). Two main metal mixtures were used: those of M. Asplund et al. (2009) and of N. Grevesse & A. J. Sauval (1998). Mass, metallicity, and initial helium abundance were all treated as free parameters by all teams. Table 2 lists the detailed configurations as well as the derived stellar parameters by each team.

Overall, the derived stellar properties for HD 219134 show strong consistency across modeling teams, despite intentional variations in input physics. The standard deviation of median values from each team is comparable to or smaller than the average uncertainties reported by each team, indicating that model uncertainties arising from differences in input physics and stellar evolution codes are generally smaller than the formal uncertainties reported.

We report our stellar properties of HD 219134 as follows: we adopted the median values and the statistical uncertainties from Team 1's median and formal uncertainty, and adopted the standard deviation of median values from each team as an estimate of the systematic uncertainties. The results are reported in Table 3 and Figure 4. We find a mass of $M_\star = 0.763 \pm 0.020(\mathrm{stat}) \pm 0.007(\mathrm{sys})$ $\mathrm{M}_\odot$, a radius of $R_\star = 0.748 \pm 0.007(\mathrm{stat}) \pm 0.002(\mathrm{sys})$ $\mathrm{R}_\odot$, an age of $t_\star = 10.151 \pm 1.520(\mathrm{stat}) \pm 0.810(\mathrm{sys})$ Gyr, and an initial helium abundance of $Y_{\mathrm{init}} = 0.27 \pm 0.02(\mathrm{stat}) \pm 0.01(\mathrm{sys})$. The fractional uncertainties of mass, radius, and age are 3%, 1%, and 18%, respectively.

The derived Y_{init} is close to the solar initial helium abundance (≈0.27; M. Asplund et al. 2009). Given that HD 219134's metallicity is also close to solar, this Y_{init} aligns well with expectations from Galactic enrichment laws (e.g., K. Verma et al. 2019; A. J. Lyttle et al. 2021).

Furthermore, we determine a stellar density of $\rho_\star = 1.823 \pm 0.003(\mathrm{stat}) \pm 0.003(\mathrm{sys})$ $\rho_\odot$, and a surface gravity of $\log g_\star = 4.577 \pm 0.001(\mathrm{stat}) \pm 0.003(\mathrm{sys})$ dex. The systematic uncertainties are comparable to or larger than the statistical uncertainties, highlighting the need to account for both sources of error for these properties (e.g. D. Huber et al. 2022).

3.3. *Asteroseismic Age is Insensitive to the Chosen Surface Physics*

Our estimate of the asteroseismic age ($t_\star = 10.151 \pm 1.520(\mathrm{stat}) \pm 0.810(\mathrm{sys})$ Gyr) is approximately 1-σ lower than the age derived by M. Gillon et al. (2017), who reported $t_\star = 11.0 \pm 2.2$ Gyr based on modeling that incorporated a precise interferometric radius.

Unlike the interferometric approach, the asteroseismic age determination is primarily based on the star's internal structure, particularly the hydrogen-burning processes near the core. This makes it less influenced by assumptions in surface modeling. This robustness is shown from the small age variations observed despite differences in surface boundary treatments applied by each team. We also confirmed that the derived frequency ratios r_{02} and r_{13} from models agree with observed values. Additionally, team 1 and 3 evaluated the effects of varying input classical observables, either using T_{eff} alone or combining T_{eff} with the interferometric radius from R. Ligi et al. (2019), and found that the resulting ages remained consistent within the quoted uncertainties.

4. RADIUS INFLATION

In Table 3 and Figure 4, we list the asteroseismic radius derived in this study with the interferometric radius determined by A. Elliot et al. (2025). The asteroseismic radius derived for HD 219134, $R_\star = 0.748 \pm 0.007(\mathrm{stat}) \pm 0.002(\mathrm{sys})$ $\mathrm{R}_\odot$, is significantly lower than the new interferometric radius, $R_\star = 0.783 \pm 0.005$ $\mathrm{R}_\odot$ (A. Elliot et al. 2025). Both radii are highly precise, with uncertainties below 1%, yet they differ by approximately 4% (a 4σ discrepancy).

While the exact cause of this discrepancy is still unclear, in this section, we explore several explanations. Future observations of more targets common to both asteroseismology and interferometry could help identify the source of this discrepancy.

4.1. *Systematic Uncertainties in Interferometry*

Interferometric visibilities can be affected by systematic errors due to assumed calibrator diameters, wavelength calibration, or limb-darkening corrections (e.g. G. T. van Belle & G. van Belle 2005). Systematic differences in interferometric angular diameters measured using different methods and instruments can reach up to 10% (T. R. White et al. 2018; J. Tayar et al. 2022). These systematic errors are most significant if the angular diameter of a target star is not well resolved compared to the calibrator diameters, which is supported

by systematic trends between photometric and interferometric temperature scales (L. Casagrande et al. 2014).

R. Ligi et al. (2019) used the optical VEGA beam combiner (D. Mourard et al. 2011) on the CHARA Array (H. A. McAlister et al. 2005) to measure the angular diameter of for HD 219134 using baselines up to ≈ 100 m, yielding a minimum visibility of $V^2 \approx 0.2-0.3$. The latest interferometric data obtained using the optical PAVO beam combiner on the CHARA Array (M. J. Ireland et al. 2008) used a longer baseline up to ≈ 160 m, thus better resolving the star down to the first visibility null (D. Huber 2016; A. Elliot et al. 2025). This makes the derived angular diameter essentially independent of systematics due to assumed calibrator sizes. Systematic effects due to limb darkening corrections and wavelength calibration are expected to be well below the 1% level (D. Huber 2012; D. Huber et al. 2012). Given previous good agreement between PAVO and VEGA for stars that are similarly well resolved (R. Ligi et al. 2012; T. R. White et al. 2013), we conclude that it is unlikely that the $\approx 4\%$ radius tension between interferometry and asteroseismology can be attributed to systematic errors in the interferometric measurements. Systematic errors in parallax scales by Gaia at this level can also be ruled out (M. A. T. Groenewegen 2021).

4.2. *Atmospheric Boundary Conditions*

We note that the majority of the asteroseismic constraints presented in this work are explicitly constructed to be insensitive to the surface (and therefore radius) of the star. This is because modeling errors — arising from the neglect of more realistic equilibrium structures in the stellar atmosphere, and the interaction between convection and oscillations — are known to produce a systematic offset between frequencies of actual stars, and those of notional 1D stellar models with identical internal structures. Corrections for this "surface effect" must therefore be applied to model frequencies, in order to mitigate this discrepancy, but doing so often renders these asteroseismic constraints insensitive to the structure of the near-surface layers through the introduction of additional free parameters. Under these circumstances, the reported radius does not depend significantly on the precise form chosen to describe this surface effect using free parameters (B. Nsamba et al. 2018; J. M. J. Ong et al. 2021). Moreover, Team 2 specifically replaced their use of the calibrated T. Sonoi et al. (2015) formulation (without free parameters) with that of W. H. Ball & L. Gizon (2014) (which does possess free parameters), and observed only a small radius reduction of 0.001 $R_\odot$.

Conversely, this means that the radius estimates returned from these asteroseismic modeling efforts are primarily model-dependent, in that they are the radii of 1D models possessing interior structures consistent with the asteroseismic constraints, rather than radii directly constrained using seismology. All else being equal, the radii of 1D models in turn are determined by the atmospheric boundary conditions imposed on them computationally.

The modeling teams employed several analytical model atmospheres, such as those utilizing T-τ relations, including Eddington's (A. S. Eddington 1926) and Krishna-Swamy's (K. S. Krishna Swamy 1966) formulation. In addition, pre-computed atmosphere tables based on more realistic 1D or 3D modes were also used (P. H. Hauschildt et al. 1999a,b; F. Castelli & R. L. Kurucz 2003; R. Trampedach et al. 2014). Furthermore, Team 4 tested the impact of replacing A. S. Eddington (1926)'s T-τ relation with that of K. S. Krishna Swamy (1966), and found a slight radius decrease of 0.009 $R_\odot$. Similarly, Team 1 replaced photosphere tables (P. H. Hauschildt et al. 1999a,b; F. Castelli & R. L. Kurucz 2003) with the A. S. Eddington (1926) model, and found a slight radius decrease of 0.006 $R_\odot$. Despite this deliberately large variety of approaches, the resulting differences in the predicted radius across the modeling teams remain small.

These findings suggest that the choice of atmospheric boundary conditions and surface correction procedure fails to explain the radius discrepancy.

4.3. *Mixing Lengths*

The radii of 1D stellar models with convective envelopes are determined by convective mixing-length theory, which specifies the temperature stratification of the superadiabatic layers close to the stellar surface. Since most of our modeling teams treated the mixing length parameter $\alpha_{\rm MLT}$ either as a global free parameter or a fixed one according to calibrations against the Sun, incorrect values of $\alpha_{\rm MLT}$ might have systematically biased the resulting asteroseismic model radius constraints.

3D hydrodynamical simulations produce entropy profiles associated with this temperature stratification that cannot be reproduced in 1D stellar evolution when $\alpha_{\rm MLT}$ is treated as a globally constant quantity. Calibrated prescriptions for $\alpha_{\rm MLT}$ also exist (e.g. F. Spada et al. 2021; R. Trampedach et al. 2014), anchored to relations between the adiabatic entropy, surface gravity, and effective temperature that are seen to emerge in these simulations (Z. Magic et al. 2015; J. D. Tanner et al. 2016). One modeling team (Team 5) performed their modeling using the variable-$\alpha_{\rm MLT}$ prescription of R. Trampedach et al. (2014), but the radius and age scale of this model-

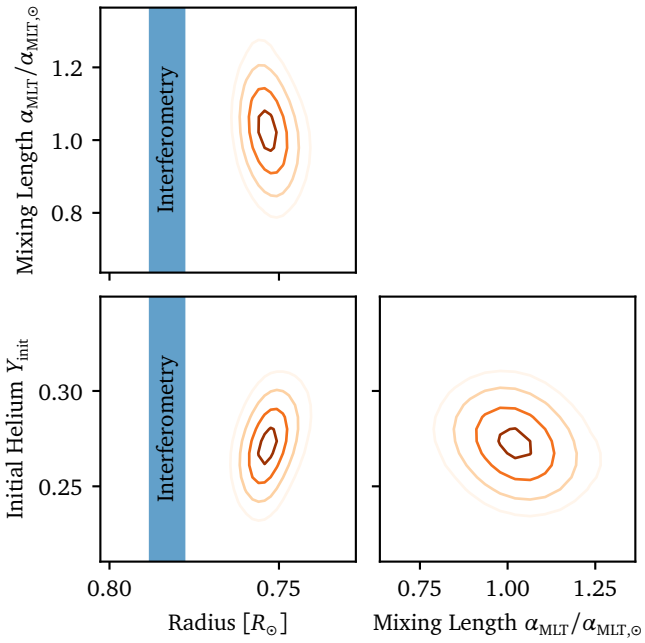

Figure 5. Probability contours of stellar properties presented in the space of radius, α_{MLT} and Y_{init}. These contours are derived from constraints provided by asteroseismic observations.

ing was still ultimately determined by a solar-calibrated value of $\alpha_{MLT} = 1.83$, against which the local α_{MLT} was obtained by scaling under this prescription.

There have also been suggestions that α_{MLT} should change as a function of stellar mass and/or metallicity in main-sequence dwarfs. 3D simulations indicate that the entropy jump between the bottom and top of the super-adiabatic region is smaller for cooler dwarfs (R. Trampedach et al. 2013). This trend corresponds to higher convective efficiency and, consequently, a larger α_{MLT} (Z. Magic et al. 2015). These suggest that $\alpha_{MLT}/\alpha_{MLT,\odot}$ at 4800 K is between 0.95 and 1.10 (R. Trampedach et al. 2014; Z. Magic et al. 2015), consistent with 2D simulations using gray radiative transfer (H.-G. Ludwig et al. 1999).

1D stellar models, when constrained by oscillation frequencies and atmospheric parameters, can also provide estimates of α_{MLT} (e.g., L. S. Viani et al. 2018). Observations of the well-characterized visual binary system α Cen A and B further support the trend of increasing α_{MLT} with decreasing stellar mass (M. Joyce & B. Chaboyer 2018), even though the fit of α_{MLT} in 1D models allows the compensation for other deficiencies in the underlying model physics.

These studies all support the notion that α_{MLT} at 4800 K should be near or slightly above solar. Accordingly, we investigate the shift of radius as a response to changing α_{MLT}. Figure 5 presents the posterior distributions of radius, α_{MLT}, and initial helium abundance (Y_{init}) using Team 1's stellar models. We see a correlation between α_{MLT} and radius. Allowing a 20% change in α_{MLT} from the best-fitting value still fails to reconcile the predicted radius with that derived from interferometry. Furthermore, larger values of α_{MLT} reduce Y_{init} to values near or below the primordial helium abundance of 0.249 (Planck Collaboration et al. 2016), which is physically implausible.

Furthermore, the use of different input physics (investigated by this paper) is unlikely to shift α_{MLT} significantly. We see near-solar α_{MLT} across modeling teams where α_{MLT} was treated as a free parameter: averaging around $\alpha_{MLT}/\alpha_{MLT\odot} = 0.980 \pm 0.053$. We also found that the α_{MLT} values persisted regardless of the boundary condition choice. This is supported by comparing the results from switching boundary condition only: Team 1 repeated their analysis replacing their photosphere tables with the A. S. Eddington (1926) boundary condition, and Team 4 repeated theirs replacing the A. S. Eddington (1926) boundary condition with that of K. S. Krishna Swamy (1966). Both teams found the variations in $\alpha_{MLT}/\alpha_{MLT\odot}$ are within their quoted 1-σ uncertainties.

4.4. *Magnetic Fields*

K and M dwarfs are often observed to have larger radii than those predicted by stellar models, a phenomenon referred to as radius inflation (G. Torres 2013). This discrepancy can be resolved in models by incorporating magnetic fields directly in stellar structure equations (G. A. Feiden & B. Chaboyer 2012; J. MacDonald & D. J. Mullan 2012; G. A. Feiden & B. Chaboyer 2013), or by including starspots that inhibit energy transport on the stellar surface (G. Somers & M. H. Pinsonneault 2015). Observational evidence suggests that the degree of radius inflation correlates with surface magnetic field strength (R. Kiman et al. 2024) and rotation period (A. C. Lanzafame et al. 2017), supporting the role of magnetic activity as a key factor.

Modeling studies found that strong magnetic fields are necessary to account for radius inflation. G. Somers & M. H. Pinsonneault (2015) found that a 50% spot coverage is required to explain a 4% radius difference (see their Figure 2). G. A. Feiden & B. Chaboyer (2013) studied UV Psc B, which shows a 10% radius inflation compared to non-magnetic models, requiring surface magnetic fields of approximately 4 kG to match the observations.

However, HD 219134 appears not to possess a magnetic field strong enough to explain the observed discrepancy. The surface magnetic field strength measured

by C. P. Folsom et al. (2018) is on the order of 2.5 G, comparable to the Sun and the α Cen A and B systems (G. A. Feiden & B. Chaboyer 2012). Furthermore, observations of the star's chromospheric emission using Ca II H and K lines spanning over a decade (see §5.4) places HD 219134 firmly in the inactive regime of stellar activity distribution. Thus, magnetic activity is very unlikely to account for the 4% difference between the asteroseismic and interferometric radii.

4.5. *Tidal Heating*

The orbital angular momentum of a planet can drive tidal interactions within the convective envelope of its host star, leading to energy dissipation in the form of heat. This dissipation can act as an additional energy source, potentially contributing to the inflation of the host star. However, in the case of HD 219134, which hosts two ultra-short-period super-Earths, HD 219134b and HD 219134c, the expected tidal effect is insufficient to account for a 4% increase in the stellar radius.

To examine this, we calculated the tidal decay timescale τ_d, for a slowly rotating host star using the following expression (J. N. Winn et al. 2018; P. Goldreich & S. Soter 1966; F. Dai et al. 2024):

$$\tau_d \approx 30\ \mathrm{Gyr} \left(\frac{Q'_\star}{10^6}\right) \left(\frac{M_\star/\mathrm{M}_\odot}{M_p/\mathrm{M}_\oplus}\right) \left(\frac{\rho_\star}{\rho_\odot}\right)^{5/3} \left(\frac{P_{\rm orb}}{1\ \mathrm{day}}\right)^{13/3}, \quad (5)$$

where $Q'_\star$ is the tidal quality factor which we assume to be 10^7 (K. Penev et al. 2018), and $P_{\rm orb}$ is the orbital period. Using this timescale, we derived the corresponding energy dissipation rate:

$$\dot{E} = \frac{3}{2} \frac{G M_\star M_p}{P_{\rm orb}} \frac{1}{\tau_d}. \quad (6)$$

With the stellar and planetary parameters from Table 3 and M. Gillon et al. (2017), we determined that the energy dissipation induced by the close-in planet HD 219134b is 1.17×10^{-7} $\mathrm{L}_\odot$. Even if all this dissipated energy were converted into stellar luminosity, it would still fall several orders of magnitude short of explaining the required 8% luminosity discrepancy (corresponding to the 4% difference in radius).

5. EVOLUTION OF ROTATION AND ACTIVITY

Using the estimated asteroseismic age, $t_\star = 10.2 \pm 1.5(\mathrm{stat}) \pm 1.0(\mathrm{sys})$ Gyr, alongside an independently measured rotation period, we can test the theory of angular momentum loss.

5.1. *Rotation Period*

Based on Calcium H and K line emission measured with HARPS-N over three years, F. Motalebi et al. (2015) reported a rotation period $P_{\rm rot} = 43.2$ d. Similarly, C. P. Folsom et al. (2018), using Zeeman–Doppler imaging from Narval spectropolarimeter, found a rotation period of $P_{\rm rot} = 42$ d. The spread in rotation period estimates from different methods is consistent with expected effects of latitudinal differential rotation. Here, we used HIRES and APF data collected via California Planet Search (L. J. Rosenthal et al. 2021; H. Isaacson et al. 2024), as well as HARPS data (F. Motalebi et al. 2015) to determine the star's rotation period. These data are shown in Figure 6. We modeled the time series using a hierarchical model and Gaussian processes. Each time series was assigned a single rotation period, with all periods assumed to follow a normal distribution with a common mean. As a result, we determined a rotation period of $P_{\rm rot} = 41 \pm 2.4$ d.

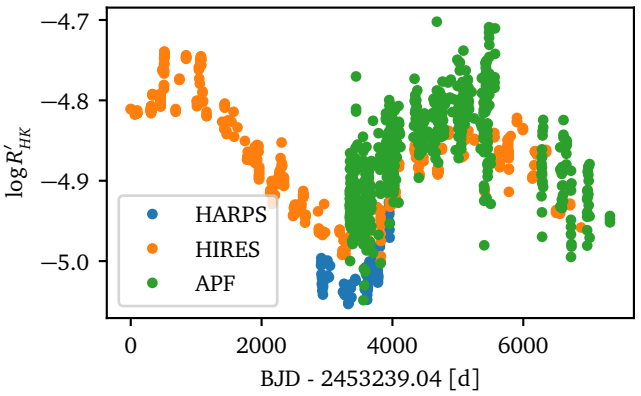

Figure 6. Time series of $\log R'_{\rm HK}$ measured by three different instruments spanning 20 years (HARPS, F. Motalebi et al. 2015; HIRES and APF, L. J. Rosenthal et al. 2021; H. Isaacson et al. 2024).

Figure 7 shows the position of this star on the $P_{\rm rot}$–$T_{\rm eff}$ plane, compared with other stars of known rotation period and benchmark ages derived from open clusters or asteroseismology. Stellar angular momentum loss over time is driven primarily by magnetized stellar winds. Establishing a well-calibrated rotation-age relationship is essential for age-dating cool dwarf stars, especially for exoplanet hosts. HD 219134 is noteworthy for occupying a unique parameter space as the coolest benchmark star with an age exceeding 4.2 Gyr.

5.2. *Rotation Modeling*

To check if our current knowledge of magnetic braking and angular momentum transport is sufficient to explain the rotation period of HD 219134 at 10.151 Gyr, we used the stellar evolution models calculated from Team 1, and calculated stellar rotation using `ROTEVOL` (J. L. van Saders & M. H. Pinsonneault 2013; G. Somers et al. 2017).

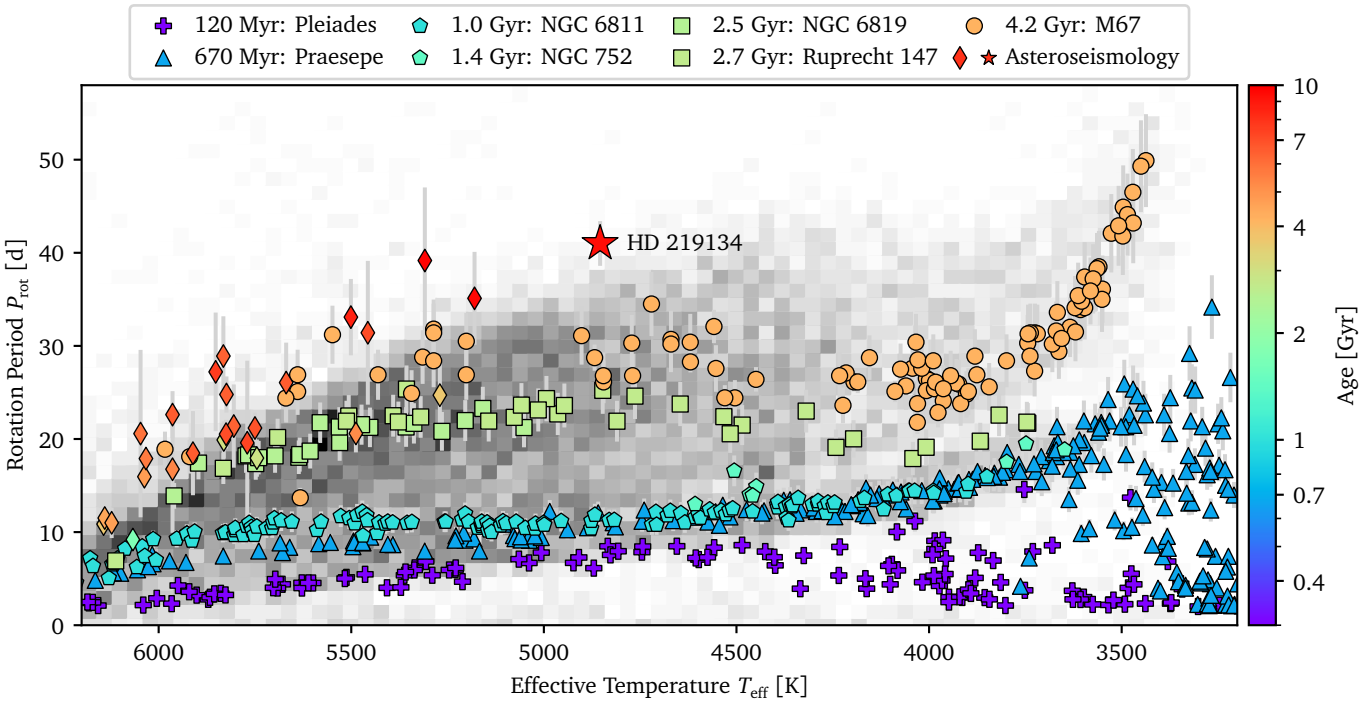

Figure 7. Calibrators of gyrochrones shown on the $P_{\rm rot}$–$T_{\rm eff}$ diagram. The open cluster data include Pleiades (L. M. Rebull et al. 2016), Praesepe (S. T. Douglas et al. 2017, 2019), NGC 6811 (J. L. Curtis et al. 2019), NGC 752 (M. A. Agüeros et al. 2018), NGC 6819 (S. Meibom et al. 2015), Ruprecht 147 (J. L. Curtis et al. 2020), and M67 (S. A. Barnes et al. 2016; R. Dungee et al. 2022; L. Long et al. 2023). The asteroseismic field stars shown include stars with both rotation periods and ages measured via asteroseismology (O. J. Hall et al. 2021; V. Silva Aguirre et al. 2015, 2017). The background displays a binned distribution of the Kepler field star sample (A. McQuillan et al. 2014). HD 219134 is the coolest age calibrator for stars older than 4.2 Gyr.

Models are initialized with a rotation period of $P_{\rm disk} = 4$ d and disk-locking timescale of $\tau_{\rm disk} = 10$ Myr, following the choices of F. Chiti et al. (2024). We employed a magnetic braking model based on J. L. van Saders et al. (2016), which quantifies the total angular momentum loss as:

$$\frac{{\rm d}J_{\rm tot}}{{\rm d}t} = \begin{cases} f_K K_M \omega_e \left(\dfrac{\omega_{\rm sat}}{\omega_\odot}\right)^2, & \omega_{\rm sat} \le \omega_e \dfrac{\tau_{\rm cz}}{\tau_{\rm cz,\odot}}, {\rm Ro} \le {\rm Ro}_{\rm crit} \\ f_K K_M \omega_e \left(\dfrac{\omega_e \tau_{\rm cz}}{\omega_\odot \tau_{\rm cz,\odot}}\right)^2, & \omega_{\rm sat} > \omega_e \dfrac{\tau_{\rm cz}}{\tau_{\rm cz,\odot}}, {\rm Ro} \le {\rm Ro}_{\rm crit} \\ 0, & {\rm Ro} > {\rm Ro}_{\rm crit} \end{cases} \tag{7}$$

Here, ω_e is the envelope rotation rate, $\tau_{\rm cz}$ is the convective overturn timescale, calculated locally at one pressure scale height above the bottom of the outer convection zone, $\omega_{\rm sat} = 3.863 \times 10^{-5}$ rad s^{-1} is the saturation threshold of angular momentum loss, Ro is the Rossby number defined as $P_{\rm rot}/\tau_{\rm cz}$ as a means to estimate stellar magnetism, and ${\rm Ro}_{\rm crit}$ is a Rossby threshold, beyond which no angular momentum loss occurs (J. L. van Saders et al. 2016; N. Saunders et al. 2024). The factor K_M scales with stellar properties as:

$$\frac{K_M}{K_{M,\odot}} = c \left(\frac{R}{R_\odot}\right)^{3.1} \left(\frac{M}{M_\odot}\right)^{-0.22} \left(\frac{L}{L_\odot}\right)^{0.56} \left(\frac{P_{\rm phot}}{P_{\rm phot,\odot}}\right)^{0.44}, \tag{8}$$

where c corrects for centrifugal force (assumed to be 1), and $P_{\rm phot}$ denotes the photospheric pressure.

We modeled the stellar rotation using a two-zone model, with the core and envelope rotating independently as solid bodies, and exchanging angular momentum over a coupling timescale $\tau_{\rm ce}$. This timescale scales with stellar mass as $\tau_{\rm ce}/\tau_{\rm ce,\odot} = (M/M_\odot)^{-\alpha_{\rm ce}}$, with $\tau_{\rm ce,\odot} \approx 22$ Myr (F. Spada & A. C. Lanzafame 2020). The angular momentum loss rates for the core and envelope are expressed as (P. A. Denissenkov et al. 2010)

$$\frac{{\rm d}J_c}{{\rm d}t} = -\frac{(\Delta J)_{\rm max}}{\tau_c} - \omega_s \frac{{\rm d}I_e}{{\rm d}t}, \tag{9}$$

$$\frac{{\rm d}J_e}{{\rm d}t} = \frac{(\Delta J)_{\rm max}}{\tau_c} + \omega_s \frac{{\rm d}I_e}{{\rm d}t} + \frac{{\rm d}J_{\rm tot}}{{\rm d}t}, \tag{10}$$

where I_e and I_c represent envelope and core inertia, respectively. The term ω_s is defined as the envelope rotation rate ω_e if the envelope is contracting, or the core rotation rate ω_c if the envelope is expanding. The maximum angular momentum exchange between the core

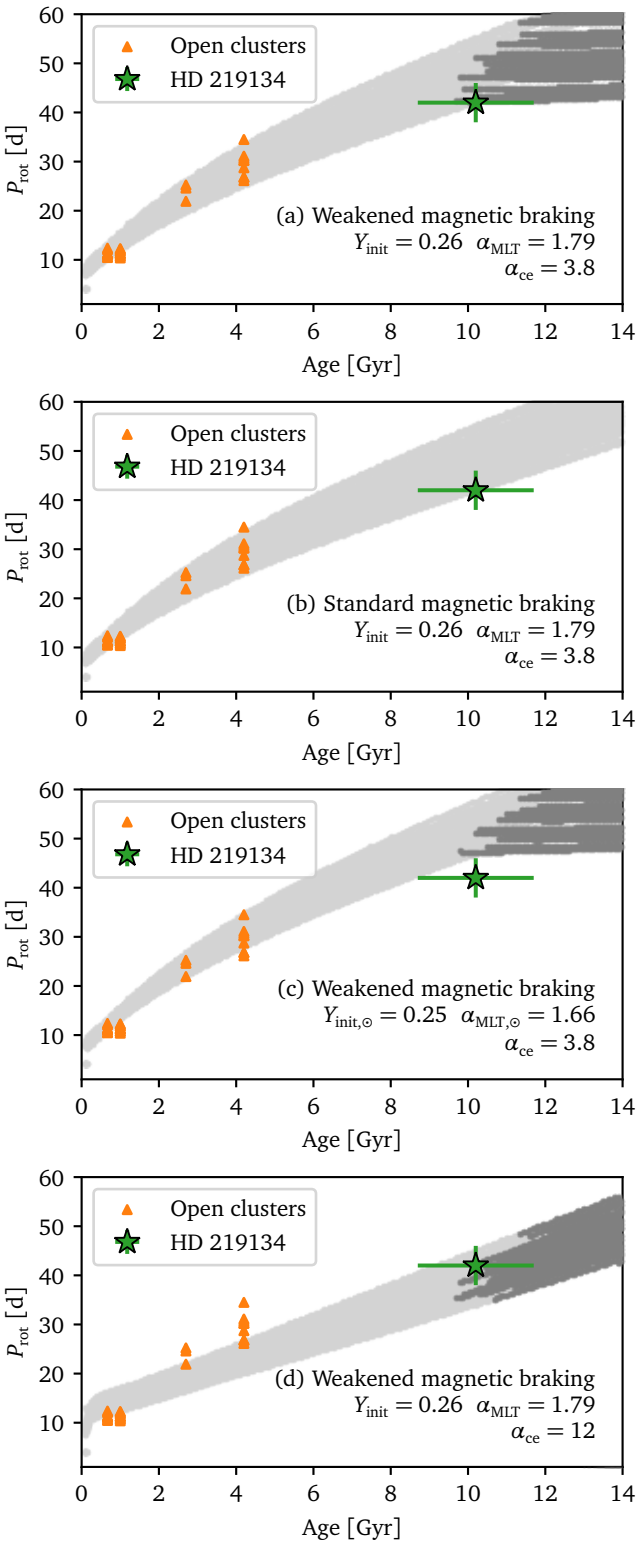

Figure 8. Rotation evolutionary models projected to older ages. These are calibrated based on asteroseismic field stars and open clusters hotter than 4500 K. The calibrators within the $T_{\rm eff} \in [4650, 4900]$ K range are shown in triangles. The evolutionary tracks include models within 3-σ that match HD 219134's mass and metallicity. Additional model configurations are specified in each panel. Models highlighted in dark gray represent those that have entered the weakened magnetic braking phase ($dJ_{\rm tot}/dt = 0$).

and envelope is given by:

$$(\Delta J)_{\rm max} = \frac{I_c I_e}{I_c + I_e}(\omega_c - \omega_e). \quad (11)$$

The free parameters in this model are f_K, ${\rm Ro_{crit}}/{\rm Ro_\odot}$ and $\alpha_{\rm ce}$. To calibrate these parameters, we constructed a sample of open clusters, field stars, and the Sun with their rotation periods and ages. The open clusters include Pleiades (120 Myr; L. M. Rebull et al. 2016), Praesepe (670 Myr; S. T. Douglas et al. 2017, 2019), NGC 6811 (1 Gyr; J. L. Curtis et al. 2019), NGC 6819 (2.5 Gyr; S. Meibom et al. 2015), Ruprecht 147 (2.7 Gyr; J. L. Curtis et al. 2020), and M67 (4.2 Gyr; S. A. Barnes et al. 2016; R. Dungee et al. 2022; L. Long et al. 2023). The field stars are Kepler stars with rotation period (O. J. Hall et al. 2021) and asteroseismic ages (V. Silva Aguirre et al. 2015, 2017). Finally, the Sun is included as a data point with $P_{\rm rot} = 25.4$ d and $t_\odot = 4.67$ Gyr (J. N. Bahcall et al. 1995). We restricted the sample to stars with effective temperatures above 4500 K, to avoid difficulties in modeling stars around 4200 K, which has enhanced activity, and are thought to be due to shear-enhanced magnetism (e.g. L. Cao et al. 2023). The best-fitting model parameters obtained are $f_K = 5.655$, ${\rm Ro_{crit}}/{\rm Ro_\odot} = 0.93$, and $\alpha_{\rm ce} = 3.8$.

5.3. *Testing Rotation Models Beyond 4.2 Gyr*

We examine these rotational evolutionary tracks for models with the same mass and metallicity as HD 219134 by predicting rotation periods to the age of HD 219134.

Figure 8(a) presents these evolutionary tracks, calculated using the default weakened magnetic braking configuration. These models assume initial helium abundance ($Y_{\rm init}$) and mixing length parameter ($\alpha_{\rm MLT}$) constrained by asteroseismology, along with the best-fitting core-envelope coupling coefficient ($\alpha_{\rm ce}$). The models agree very well with HD 219134's observed rotation period and age. The estimated ${\rm Ro}/{\rm Ro_\odot}$ is 0.83±0.07, only slightly below the critical value ${\rm Ro_{crit}}/{\rm Ro_\odot} = 0.93$, indicating the star is around the transition point into the weakened magnetic braking regime.

H. Isaacson et al. (2024) reported an activity cycle of $P_{\rm cyc} = 13.27$ yr for HD 219134, placing it on the lower sequence in the $P_{\rm cyc}$–$P_{\rm rot}$ diagram. Following T. S. Metcalfe et al. (2022), this positioning also implies HD 219134 is close to the transition into weakened magnetic braking (J. L. van Saders et al. 2016), consistent with our findings.

In fact, T. Metcalfe et al. (2025) found evidence of significantly weakened instantaneous torque in HD 219134, based on constraints on magnetic field strength and mor-

phology from ZDI, suggesting the star has already entered the weakened magnetic braking phase. Given that our estimate of $\mathrm{Ro}/\mathrm{Ro}_\odot$ is 1σ below $\mathrm{Ro}_{\mathrm{crit}}/\mathrm{Ro}_\odot$, this provides tentative (though not statistically significant) evidence that $\mathrm{Ro}_{\mathrm{crit}}$ for this star may be different from most G-dwarf asteroseismic calibrators.

We also modeled rotational evolution assuming standard magnetic braking, which prescribes continued spin-down even when $\mathrm{Ro} > \mathrm{Ro}_{\mathrm{crit}}$ (modifying the third line in Equation 7 to equal the second line). The results are shown in Figure 8(b). As expected, this model predicts further spin-down beyond 10 Gyr. If the observation of instantaneous torque is not considered, both the standard and weakened braking models adequately explain the current observations. This is because the divergence in rotation periods between the two regimes requires a longer timescale to become clearly distinguishable.

Next, we tested whether models with solar-calibrated Y_{init} and α_{MLT} could also explain the observations. These results are shown in Figure 8(c). Compared with Figure 8(a), models with Y_{init} and α_{MLT} constrained by asteroseismology provide a better overall fit. The initial helium abundance (Y_{init}) affects the stellar structure by altering the size of the convection zone, and hence τ_{cz} (N. Saunders et al. 2024), similar to the effects of [Fe/H] or [α/M] (Z. R. Claytor et al. 2020). This highlights the importance of incorporating detailed chemical abundances for accurately predicting ages using gyrochronology.

Finally, we explored models with a large coupling timescale motivated by studies such as L. Cao et al. (2023), who found $\alpha_{\mathrm{ce}} \approx 12$ for late K dwarfs with enhanced magnetism in the Praesepe open cluster. These models are presented in Figure 8(d). While the rotation period and age of HD 219134 agree with the model, the rotation period for stars around 3 Gyr is underestimated. Thus, our data do not support a larger coupling timescale for stars at this T_{eff}. This suggests that the scaling relation for coupling timescale versus mass may be oversimplified for modeling the stalled spin-down phase.

In summary, weakened magnetic braking models with constrained abundances provide a strong match to HD 219134's observed rotation period and asteroseismic age. Our findings support the reliability of such models for predicting rotational evolution in early K-type dwarfs beyond 4.2 Gyr. The effects of prolonged core-envelope coupling earlier in stellar evolution can leave observable imprints in older stars. Combining asteroseismic ages and torque measurements for a statistically significant sample will help constrain the coupling timescale as a function of T_{eff}.

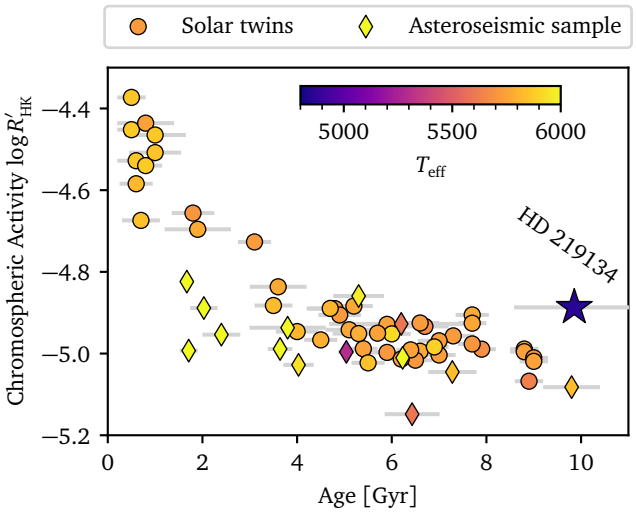

Figure 9. Chromospheric activity-age relation. The sample includes solar twins (D. Lorenzo-Oliveira et al. 2018), the Kepler asteroseismic sample (C. Karoff et al. 2013; T. S. Metcalfe et al. 2016; O. L. Creevey et al. 2017), and the TESS asteroseismic sample (D. Huber et al. 2022; A. Chontos et al. 2021; T. S. Metcalfe et al. 2020, 2021)

5.4. *Activity-Age Relations*

A common method for age-dating field stars involves using activity-age relations. These activity indices include metrics such as spot modulation amplitudes, emissions in spectral lines (e.g., Calcium H&K and Hα), and emissions in the X-ray or radio spectrum. In this study, we examined whether the chromospheric activity of HD 219134 aligns with established activity-age relationships.

Wherever possible, we used the color-temperature relation from M. Sekiguchi & M. Fukugita (2000) and converted the S-indices into the color-independent activity index $\log R'_{\mathrm{HK}}$, on the scale defined by F. Middelkoop (1982) and R. W. Noyes et al. (1984). Figure 9 presents $\log R'_{\mathrm{HK}}$ for a sample of solar twins (D. Lorenzo-Oliveira et al. 2018) and asteroseismic samples from Kepler and TESS (C. Karoff et al. 2013; T. S. Metcalfe et al. 2016; O. L. Creevey et al. 2017; D. Huber et al. 2022; A. Chontos et al. 2021; T. S. Metcalfe et al. 2020, 2021). We found that at an age of 10 Gyr, HD 219134 exhibits a higher activity level compared to solar twins of the same age but is comparable to the activity levels observed in solar twins at 5 Gyr. This is consistent with expectations that activity levels scale with Ro, as Ro of HD 219134 is close to $\mathrm{Ro}_{\mathrm{crit}}$, a value also observed for solar twins at 5 Gyr, beyond which they enter into the phase of weakened magnetic braking. This result supports the inclusion of a T_{eff} dependence in the $\log R'_{\mathrm{HK}}$–age relation, particularly for cooler stars, as dif-

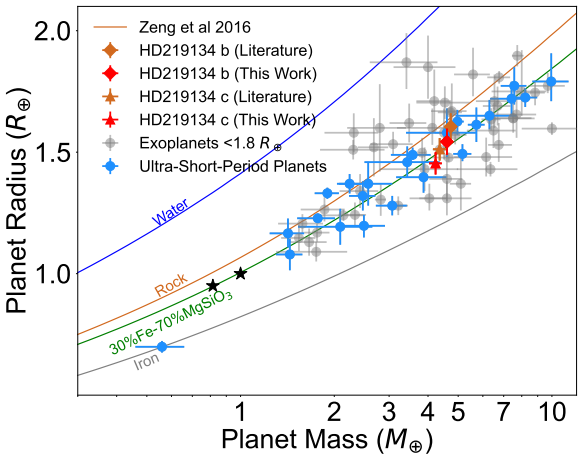

Figure 10. The mass–radius diagram of exoplanets with $R_p < 1.8$ R$_\oplus$. The solid lines represent different theoretical compositional models.

ferences in Ro can affect the activity-age trend by as much as 5 Gyr.

6. REVISING PLANET PROPERTIES

HD 219134 hosts at least five confirmed exoplanets, including two transiting super-Earths (HD 219134b and HD 219134c) first discovered by M. Gillon et al. (2017) from photometric analysis using the Spitzer Space Telescope. As one of brightest star known to host transiting planets the system has been extensively studied, including the possibility of the formation and detection of planetary exospheres (A. A. Vidotto et al. 2018).

We produce revised properties of the two transiting planets based on our new asteroseismic stellar mass and radius. The mass of transiting planets can be calculated using

$$M_p = \frac{K_1^2 + \sqrt{K_1^4 + 4G(1-e^2)^{-1}\sin^2 i\; a^{-1}K_1^2 M_\star}}{2G(1-e^2)^{-1}\sin^2 i\; a^{-1}}, \quad (12)$$

where K_1, e, i, a, G denote the RV semi-amplitude, orbital eccentricity, orbital inclination, semi-major axis, and the gravitational constant, respectively. The radius of a transiting planet is given by

$$R_p = R_\star \cdot R'_p/R'_\star, \quad (13)$$

where $R'_p/R'_\star$ is the old planet and star radius ratio determined by M. Gillon et al. (2017).

Using the orbital parameters provided in M. Gillon et al. (2017, see their Table 1) along with the asteroseismic mass and radius derived in this work, we revise the HD 219134b's mass and radius from $M_p = 4.73 \pm 0.17$ M$_\oplus$ and $R_p = 1.605 \pm 0.055$ R$_\oplus$ to $M_p = 4.59 \pm 0.16$ M$_\oplus$ and $R_p = 1.542 \pm 0.054$ R$_\oplus$. Similarly, we revise the mass and radius of HD 219134c from $M_p = 4.36 \pm 0.21$ M$_\oplus$ and $R_p = 1.512 \pm 0.046$ R$_\oplus$ to $M_p = 4.23 \pm 0.20$ M$_\oplus$ and $R_p = 1.455 \pm 0.046$ R$_\oplus$.

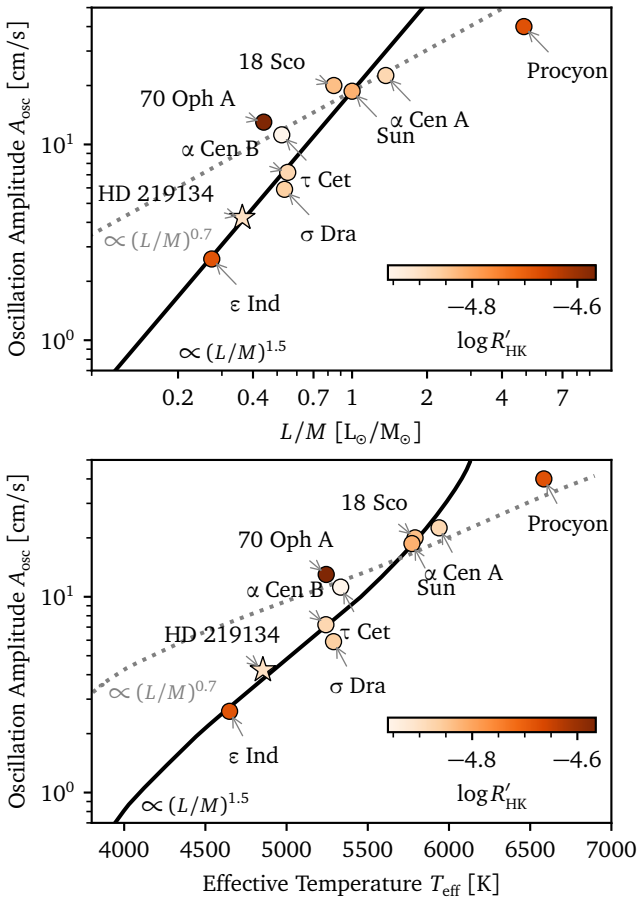

Figure 11. Oscillation amplitudes in radial velocity as a function of L/M (top) and $T_{\rm eff}$ (bottom) for main-sequence dwarfs, color-coded by chromospheric activity.

We plot both the previous and updated planet properties on the mass-radius diagram in Figure 10. The revised mass and radius shift the original data points slightly downward, supporting the hypothesis that ultra-short-period super-Earths typically exhibit an Earth-like composition of 30% Fe and 70% $MgSiO_3$ composition (C. D. Dressing et al. 2015; F. Dai et al. 2019; C. L. Brinkman et al. 2024).

7. OSCILLATION AMPLITUDES

Using `pySYD`, we measured the mode amplitude $A_{\rm osc}$ and the frequency of maximum power $\nu_{\rm max}$ from a heavily smoothed power spectrum. We obtained $A_{\rm osc} = 4.23 \pm 0.41$ cm/s, and $\nu_{\rm max} = 4651 \pm 301$ μHz.

The power spectrum of HD 219134 appears to show a dip in the center of the oscillation region that is remark-

ably similar to that seen in α Cen B, which the only other K dwarf with a high-SNR power spectrum (see Fig. 4 of H. Kjeldsen et al. 2005). Similar features are also seen in ϵ Ind (Fig. 3 of T. L. Campante et al. 2024), and σ Dra (Fig. 6 of M. Hon et al. 2024b), though based on shorter time series. It remains to be seen whether this is a real feature of K dwarfs, which would be important for our understanding of the excitation and damping mechanisms of solar-like oscillations (see review by G. Houdek & M.-A. Dupret 2015).

Figure 11 places HD 219134 among a sample of cool dwarf stars with oscillation amplitudes measured from radial velocity. The pulsation amplitude in radial velocity is theoretically expected to scale as $A_{\rm osc} \propto (L/M)^s$, with s ranging from 0.7 to 1.5 (J. Christensen-Dalsgaard & S. Frandsen 1983; H. Kjeldsen & T. R. Bedding 1995; G. Houdek et al. 1999; R. Samadi et al. 2007). Figure 11 also overlays MIST isochrones (J. Choi et al. 2016) to illustrate the relationship between $A_{\rm osc}$ and $T_{\rm eff}$, assuming $A_{\rm osc}$ scales with (L/M) at power indices of 0.7 and 1.5, evaluated at ages of 1 and 4.6 Gyr, respectively. While an s index of 0.7 is consistent with observations of G- and F-type stars, T. L. Campante et al. (2024) first suggested that cooler stars, such as ϵ Indi, align more closely with $s \approx 1.5$. Our analysis of HD 219134 supports this result.

It has also been proposed that higher stellar activity can reduce oscillation amplitudes. However, despite HD 219134 and τ Ceti being relatively inactive, they follow the $s \approx 1.5$ relation, indicating that activity alone is unlikely to account for the steeper amplitude scaling observed in cooler stars.

8. DISCUSSION AND CONCLUSION

In this work, we present an asteroseismic analysis of HD 219134 using 4 consecutive nights of radial velocity data obtained with Keck Planet Finder on Keck-I. We used the Gold deconvolution algorithm to disentangle the power spectrum from the spectral window, in order to permit identification of modes separated by close to 1 c/d, coinciding with the characteristic spacing of sidelobes. A total of 25 oscillation modes with spherical degrees $0 \leq \ell \leq 3$ were identified and extracted, as summarized in Table 1. We then estimated HD 219134's properties using five independent asteroseismic modeling pipelines. The resulting parameters are: mass 0.763 ± 0.020 (stat) ± 0.007 (sys) $M_\odot$, radius 0.748 ± 0.007 (stat) ± 0.002 (sys) $R_\odot$, and age 10.151 ± 1.520 (stat) ± 0.810 (sys) Gyr. These in turn led to revised masses and radii of the known transiting planets orbiting HD 219134, as detailed in Table 3.

Asteroseismology with EPRV instruments is a promising avenue for calibrating gyrochronology and studying angular momentum loss in old K and M dwarfs. HD 219134 in particular is the first dwarf cooler than 5000 K with an asteroseismic age estimate available. We used this to test models of rotational evolution used for this purpose by confronting them, at this age, with an independent measurement of its present rotational period. We demonstrated that existing models of angular momentum loss, incorporating weakened magnetic braking and asteroseismically constrained values of $Y_{\rm init}$ and $\alpha_{\rm MLT}$, accurately reproduce HD 219134's rotation period at its asteroseismic age. We further found that the spin-down relation for stars at this temperature requires a shorter spin-down coupling timescale than those suggested for late K dwarfs.

Nonetheless, we note that this agreement, and ultimately the apparent robustness of our asteroseismic age estimate, requires that our evolutionary stellar modeling be accurate. Such an assumption of accuracy in modeling also fundamentally underpins our asteroseismic radius constraints, since these are (as we discuss in §4.2) the radii of stellar models consistent with asteroseismic constraints on stellar interiors, rather than stellar radii directly constrained using asteroseismology. Importantly, we have also found our asteroseismic radius to be 4% smaller than the interferometric radius at 4-σ level, possibly indicating some deficiency in the accuracy of this modeling. We were unable to easily attribute this discrepancy to any systematic uncertainties related to interferometry, nor to variations in canonical choices of atmospheric boundary conditions or mixing length theory used in stellar modeling, nor to magnetic fields, nor tidal heating. Without any insight into the cause of this discrepancy, our subsequently derived quantities, and treatment of rotational evolution — all of which are contingent on these model ages and radii — must necessarily be regarded as being only conditional, pending a better understanding of the physical origin for this discrepancy. Future direct constraints on stellar radii from asteroseismology (e.g. through potential breakthroughs in understanding and mitigating the surface term) may alleviate this dependence on evolutionary modeling.

Finally, we have confirmed that HD 219134's oscillation mode amplitudes scale with those of other cool dwarfs as $(L/M)^{1.5}$, deviating from the $(L/M)^{0.7}$ relation observed in G-type stars. Should this difference in scaling behaviour be genuine and general, this may have important implications for the interpretation of other asteroseismic observables, namely $\nu_{\rm max}$, in similar stars. In particular, both the oscillation amplitudes and $\nu_{\rm max}$ are thought to be fully determined by the properties of

turbulent stresses in the near-surface layers — both ultimately reflect the physical processes that excite normal modes to visible amplitudes in the first place. If the convective turbulence that operates G-type stars should indeed be fundamentally different in some fashion from in cooler dwarfs — yielding oscillation amplitudes that scale differently in these two classes of stars — then we might also expect a different $\nu_{\rm max}$ scaling relation to be required for these cooler dwarfs. Suggestively, HD 219134 joins α Cen B (H. Kjeldsen et al. 2005), ϵ Ind (T. L. Campante et al. 2024), and σ Dra (M. Hon et al. 2024b), in appearing to exhibit an asymmetric excitation envelope, and a local minimum in mode amplitudes close to $\nu_{\rm max}$, differing qualitatively from the solar phenomenology of a single, largely symmetric, envelope. Further, more detailed analyses of non-adiabatic pulsations and convective excitation, and a larger observational sample of likewise cool dwarfs, will be needed both to determine the exact cause of this difference, as well as to determine whether the solar-calibrated $\nu_{\rm max}$ scaling relation indeed also holds for stars with modified amplitude scaling.

ACKNOWLEDGEMENTS

The authors wish to recognize and acknowledge the very significant cultural role and reverence that the summit of Maunakea has always had within the Native Hawaiian community. We are most fortunate to have the opportunity to conduct observations from this mountain. Y.L. acknowledges support from Beatrice Watson Parrent Fellowship and a NASA Keck PI Data Award, which is administered by the NASA Exoplanet Science Institute. Data presented herein were obtained at the W. M. Keck. Observatory from telescope time allocated to the National Aeronautics and Space Administration through the agency's scientific partnership with the California Institute of Technology and the University of California. The Observatory was made possible by the generous financial support of the W. M. Keck Foundation. D.H. acknowledges support from the Alfred P. Sloan Foundation, the National Aeronautics and Space Administration (80NSSC22K0781), and the Australian Research Council (FT200100871). J.M.J.O. acknowledges support from NASA through the NASA Hubble Fellowship grant HST-HF2-51517.001, awarded by STScI. STScI is operated by the Association of Universities for Research in Astronomy, Incorporated, under NASA contract NAS5-26555. T.R.B. acknowledges support from the Australian Research Council through Laureate Fellowship FL220100117. T.L.C. is supported by Fundação para a Ciência e a Tecnologia (FCT) in the form of a work contract (CEECIND/00476/2018). M.S.L. is supported by a research grant (42101) from VILLUM FONDEN. N.S. acknowledges support by the National Science Foundation Graduate Research Fellowship Program under Grant Numbers 1842402 & 2236415 and NASA's Interdisciplinary Consortia for Astrobiology Research (NNH19ZDA001N-ICAR) under award number 19-ICAR19 2-0041.

REFERENCES

Adelberger, E. G., Austin, S. M., Bahcall, J. N., et al. 1998, Reviews of Modern Physics, 70, 1265

Aerts, C. 2021, Reviews of Modern Physics, 93, 015001

Agüeros, M. A., Bowsher, E. C., Bochanski, J. J., et al. 2018, ApJ, 862, 33

Angulo, C., Arnould, M., Rayet, M., et al. 1999, NuPhA, 656, 3

Antia, H. M., & Basu, S. 1994, A&AS, 107, 421

Asplund, M., Grevesse, N., Sauval, A. J., & Scott, P. 2009, ARA&A, 47, 481

Asplund, M., Nordlund, Å., Trampedach, R., Allende Prieto, C., & Stein, R. F. 2000, A&A, 359, 729

Auvergne, M., Bodin, P., Boisnard, L., et al. 2009, A&A, 506, 411

Bahcall, J. N., Pinsonneault, M. H., & Wasserburg, G. J. 1995, Reviews of Modern Physics, 67, 781

Bailer-Jones, C. A. L., Rybizki, J., Fouesneau, M., Demleitner, M., & Andrae, R. 2021a, AJ, 161, 147

—. 2021b, AJ, 161, 147

Ball, W. H., & Gizon, L. 2014, A&A, 568, A123

Barnes, S. A., Weingrill, J., Fritzewski, D., Strassmeier, K. G., & Platais, I. 2016, ApJ, 823, 16

Bedding, T. R., & Kjeldsen, H. 2003, PASA, 20, 203

Bedding, T. R., Kjeldsen, H., Butler, R. P., et al. 2004, ApJ, 614, 380

Bedding, T. R., Butler, R. P., Kjeldsen, H., et al. 2001, ApJL, 549, L105

Berger, T. A., Huber, D., van Saders, J. L., et al. 2020, AJ, 159, 280

Böhm-Vitense, E. 1958, ZA, 46, 108

Borucki, W. J., Koch, D., Basri, G., et al. 2010, Science, 327, 977

Bouchy, F., & Carrier, F. 2001, A&A, 374, L5

—. 2002, A&A, 390, 205

Brinkman, C. L., Weiss, L. M., Huber, D., et al. 2024, arXiv e-prints, arXiv:2410.00213

Brown, T. M., Gilliland, R. L., Noyes, R. W., & Ramsey, L. W. 1991, ApJ, 368, 599

Campante, T. L., Kjeldsen, H., Li, Y., et al. 2024, A&A, 683, L16

Cao, L., Pinsonneault, M. H., & van Saders, J. L. 2023, ApJL, 951, L49

Carrier, F., & Bourban, G. 2003, A&A, 406, L23

Carrier, F., & Eggenberger, P. 2006, A&A, 450, 695

Casagrande, L., Portinari, L., Glass, I. S., et al. 2014, MNRAS, 439, 2060

Castelli, F., & Kurucz, R. L. 2003, in IAU Symposium, Vol. 210, Modelling of Stellar Atmospheres, ed. N. Piskunov, W. W. Weiss, & D. F. Gray, A20

Chaplin, W. J., Elsworth, Y., Isaak, G. R., Miller, B. A., & New, R. 2000, MNRAS, 313, 32

Chaplin, W. J., & Miglio, A. 2013, Annual Review of Astronomy and Astrophysics, 51, 353

Chaplin, W. J., Lund, M. N., Handberg, R., et al. 2015, PASP, 127, 1038

Chiti, F., van Saders, J. L., Heintz, T. M., et al. 2024, arXiv e-prints, arXiv:2403.12129

Choi, J., Dotter, A., Conroy, C., et al. 2016, ApJ, 823, 102

Chontos, A., Huber, D., Berger, T. A., et al. 2021, ApJ, 922, 229

Christensen-Dalsgaard, J. 1984, in Space Research in Stellar Activity and Variability, ed. A. Mangeney & F. Praderie, 11

Christensen-Dalsgaard, J. 2008, Ap&SS, 316, 113

Christensen-Dalsgaard, J., & Frandsen, S. 1983, SoPh, 82, 165

Claytor, Z. R., van Saders, J. L., Santos, Â. R. G., et al. 2020, ApJ, 888, 43

Cox, J. P., & Giuli, R. T. 1968, Principles of stellar structure

Creevey, O. L., Metcalfe, T. S., Schultheis, M., et al. 2017, A&A, 601, A67

Curtis, J. L., Agüeros, M. A., Douglas, S. T., & Meibom, S. 2019, ApJ, 879, 49

Curtis, J. L., Agüeros, M. A., Matt, S. P., et al. 2020, ApJ, 904, 140

Cyburt, R. H., Amthor, A. M., Ferguson, R., et al. 2010, ApJS, 189, 240

Dai, F., Masuda, K., Winn, J. N., & Zeng, L. 2019, ApJ, 883, 79

Dai, F., Howard, A. W., Halverson, S., et al. 2024, AJ, 168, 101

Davies, G. R., Handberg, R., Miglio, A., et al. 2014, MNRAS, 445, L94

Demarque, P., Guenther, D. B., Li, L. H., Mazumdar, A., & Straka, C. W. 2008, Ap&SS, 316, 31

Denissenkov, P. A., Pinsonneault, M., Terndrup, D. M., & Newsham, G. 2010, ApJ, 716, 1269

Douglas, S. T., Agüeros, M. A., Covey, K. R., & Kraus, A. 2017, ApJ, 842, 83

Douglas, S. T., Curtis, J. L., Agüeros, M. A., et al. 2019, ApJ, 879, 100

Dressing, C. D., Charbonneau, D., Dumusque, X., et al. 2015, ApJ, 800, 135

Dungee, R., van Saders, J., Gaidos, E., et al. 2022, ApJ, 938, 118

Eddington, A. S. 1926, The Internal Constitution of the Stars

Elliot et al., A. 2025, in preparation

Feiden, G. A., & Chaboyer, B. 2012, ApJ, 761, 30

—. 2013, ApJ, 779, 183

Fischer, D. A., Anglada-Escude, G., Arriagada, P., et al. 2016, PASP, 128, 066001

Folsom, C. P., Fossati, L., Wood, B. E., et al. 2018, MNRAS, 481, 5286

Formicola, A., Imbriani, G., Costantini, H., et al. 2004, Physics Letters B, 591, 61

Gibson, S. R. 2016, in Society of Photo-Optical Instrumentation Engineers (SPIE) Conference Series, Vol. 9911, Modeling, Systems Engineering, and Project Management for Astronomy VI, ed. G. Z. Angeli & P. Dierickx, 99112C

Gibson, S. R., Howard, A. W., Roy, A., et al. 2018, in Society of Photo-Optical Instrumentation Engineers (SPIE) Conference Series, Vol. 10702, Ground-based and Airborne Instrumentation for Astronomy VII, ed. C. J. Evans, L. Simard, & H. Takami, 107025X

Gibson, S. R., Howard, A. W., Rider, K., et al. 2020, in Society of Photo-Optical Instrumentation Engineers (SPIE) Conference Series, Vol. 11447, Ground-based and Airborne Instrumentation for Astronomy VIII, ed. C. J. Evans, J. J. Bryant, & K. Motohara, 1144742

Gibson, S. R., Howard, A. W., Rider, K., et al. 2024, in Society of Photo-Optical Instrumentation Engineers (SPIE) Conference Series, Vol. 13096, Ground-based and Airborne Instrumentation for Astronomy X, ed. J. J. Bryant, K. Motohara, & J. R. D. Vernet, 1309609

Gillon, M., Demory, B.-O., Van Grootel, V., et al. 2017, Nature Astronomy, 1, 0056

Gold, R. 1964,

Goldreich, P., & Keeley, D. A. 1977, ApJ, 212, 243

Goldreich, P., & Soter, S. 1966, Icarus, 5, 375

González-Cuesta, L., Mathur, S., García, R. A., et al. 2023, A&A, 674, A106

Grevesse, N., & Sauval, A. J. 1998, SSRv, 85, 161

Groenewegen, M. A. T. 2021, A&A, 654, A20

Grundahl, F., Kjeldsen, H., Christensen-Dalsgaard, J., Arentoft, T., & Frandsen, S. 2007, Communications in Asteroseismology, 150, 300

Hacking, P., Herter, T., Stacey, C., et al. 1997, in Astronomical Society of the Pacific Conference Series, Vol. 124, Diffuse Infrared Radiation and the IRTS, ed. H. Okuda, T. Matsumoto, & T. Rollig, 432

Hall, O. J., Davies, G. R., van Saders, J., et al. 2021, Nature Astronomy, 5, 707

Hammer, J. W., Fey, M., Kunz, R., et al. 2005, NuPhA, 758, 363

Harvey, J. W. 1988, in Advances in Helio- and Asteroseismology, ed. J. Christensen-Dalsgaard & S. Frandsen, Vol. 123, 497

Hatt, E., Nielsen, M. B., Chaplin, W. J., et al. 2023, A&A, 669, A67

Hauschildt, P. H., Allard, F., & Baron, E. 1999a, ApJ, 512, 377

Hauschildt, P. H., Allard, F., Ferguson, J., Baron, E., & Alexander, D. R. 1999b, ApJ, 525, 871

Henyey, L., Vardya, M. S., & Bodenheimer, P. 1965, ApJ, 142, 841

Herwig, F. 2000, A&A, 360, 952

Høg, E., Fabricius, C., Makarov, V. V., et al. 2000, A&A, 355, L27

Hon, M., Li, Y., & Ong, J. 2024a, ApJ, 973, 154

Hon, M., Huber, D., Li, Y., et al. 2024b, arXiv e-prints, arXiv:2407.21234

Houdek, G., Balmforth, N. J., Christensen-Dalsgaard, J., & Gough, D. O. 1999, A&A, 351, 582

Houdek, G., & Dupret, M.-A. 2015, Living Reviews in Solar Physics, 12, 8

Huber, D. 2012, PhD thesis, University of Sydney, Australia

—. 2016, arXiv e-prints, arXiv:1604.07442

Huber, D., Ireland, M. J., Bedding, T. R., et al. 2012, ApJ, 760, 32

Huber, D., Zinn, J., Bojsen-Hansen, M., et al. 2017, ApJ, 844, 102

Huber, D., White, T. R., Metcalfe, T. S., et al. 2022, AJ, 163, 79

Ireland, M. J., Mérand, A., ten Brummelaar, T. A., et al. 2008, in Society of Photo-Optical Instrumentation Engineers (SPIE) Conference Series, Vol. 7013, Optical and Infrared Interferometry, ed. M. Schöller, W. C. Danchi, & F. Delplancke, 701324

Isaacson, H., Howard, A. W., Fulton, B., et al. 2024, ApJS, 274, 35

Jackiewicz, J. 2021, Frontiers in Astronomy and Space Sciences, 7, 102

Jermyn, A. S., Bauer, E. B., Schwab, J., et al. 2023, ApJS, 265, 15

Joyce, M., & Chaboyer, B. 2018, ApJ, 864, 99

Karoff, C., Metcalfe, T. S., Chaplin, W. J., et al. 2013, MNRAS, 433, 3227

Kiman, R., Brandt, T. D., Faherty, J. K., & Popinchalk, M. 2024, AJ, 168, 126

Kjeldsen, H., & Bedding, T. R. 1995, A&A, 293, 87

—. 2011, A&A, 529, L8

Kjeldsen, H., & Bedding, T. R. 2012, in IAU Symposium, Vol. 285, New Horizons in Time Domain Astronomy, ed. E. Griffin, R. Hanisch, & R. Seaman, 17–22

Kjeldsen, H., Bedding, T. R., Butler, R. P., et al. 2005, ApJ, 635, 1281

Kokori, A., Tsiaras, A., Edwards, B., et al. 2023, ApJS, 265, 4

Krishna Swamy, K. S. 1966, ApJ, 145, 174

Lanzafame, A. C., Spada, F., & Distefano, E. 2017, A&A, 597, A63

Li, Y., Bedding, T. R., Li, T., et al. 2020, MNRAS, 495, 2363

Li, Y., Bedding, T. R., Stello, D., et al. 2023, MNRAS, 523, 916

Ligi, R., Mourard, D., Lagrange, A. M., et al. 2012, A&A, 545, A5

Ligi, R., Dorn, C., Crida, A., et al. 2019, A&A, 631, A92

Lomb, N. R. 1976, Ap&SS, 39, 447

Long, L., Bi, S., Zhang, J., et al. 2023, ApJS, 268, 30

Lorenzo-Oliveira, D., Freitas, F. C., Meléndez, J., et al. 2018, A&A, 619, A73

Ludwig, H.-G., Freytag, B., & Steffen, M. 1999, A&A, 346, 111

Lund, M. N., Chaplin, W. J., Casagrande, L., et al. 2016, PASP, 128, 124204

Lund, M. N., Silva Aguirre, V., Davies, G. R., et al. 2017, ApJ, 835, 172

Lund, M. N., Basu, S., Bieryla, A., et al. 2024, A&A, 688, A13

Lundkvist, M. S., Kjeldsen, H., Bedding, T. R., et al. 2024, ApJ, 964, 110

Lyttle, A. J., Davies, G. R., Li, T., et al. 2021, MNRAS, 505, 2427

MacDonald, J., & Mullan, D. J. 2012, MNRAS, 421, 3084

Magic, Z., Weiss, A., & Asplund, M. 2015, A&A, 573, A89

Martić, M., Schmitt, J., Lebrun, J. C., et al. 1999, A&A, 351, 993

Matthews, J. M., Kuschnig, R., Walker, G. A. H., et al. 2000, in Astronomical Society of the Pacific Conference Series, Vol. 203, IAU Colloq. 176: The Impact of Large-Scale Surveys on Pulsating Star Research, ed. L. Szabados & D. Kurtz, 74–75

McAlister, H. A., ten Brummelaar, T. A., Gies, D. R., et al. 2005, ApJ, 628, 439

McQuillan, A., Mazeh, T., & Aigrain, S. 2014, ApJS, 211, 24

Meibom, S., Barnes, S. A., Platais, I., et al. 2015, Nature, 517, 589

Metcalfe, T. S., Egeland, R., & van Saders, J. 2016, ApJL, 826, L2

Metcalfe, T. S., van Saders, J. L., Basu, S., et al. 2020, ApJ, 900, 154

—. 2021, ApJ, 921, 122

Metcalfe, T. S., Finley, A. J., Kochukhov, O., et al. 2022, ApJL, 933, L17

Metcalfe et al., T. 2025, in preparation

Middelkoop, F. 1982, A&A, 107, 31

Moedas, N., Bossini, D., Deal, M., & Cunha, M. S. 2024, A&A, 684, A113

Morháč, M., & Matoušek, V. 2009, Digital Signal Processing, 19, 372

Morháč, M., Matoušek, V., & Kliman, J. 2003, Digital Signal Processing, 13, 144

Mosser, B., Maillard, J. P., Mekarnia, D., & Gay, J. 1998, A&A, 340, 457

Motalebi, F., Udry, S., Gillon, M., et al. 2015, A&A, 584, A72

Mourard, D., Bério, P., Perraut, K., et al. 2011, A&A, 531, A110

Noyes, R. W., Hartmann, L. W., Baliunas, S. L., Duncan, D. K., & Vaughan, A. H. 1984, ApJ, 279, 763

Nsamba, B., Campante, T. L., Monteiro, M. J. P. F. G., et al. 2018, MNRAS, 477, 5052

Ong, J. M. J., & Basu, S. 2019, ApJ, 885, 26

Ong, J. M. J., Basu, S., & McKeever, J. M. 2021, ApJ, 906, 54

Paxton, B., Bildsten, L., Dotter, A., et al. 2011, ApJS, 192, 3

Paxton, B., Cantiello, M., Arras, P., et al. 2013, ApJS, 208, 4

Paxton, B., Marchant, P., Schwab, J., et al. 2015, ApJS, 220, 15

Paxton, B., Schwab, J., Bauer, E. B., et al. 2018, ApJS, 234, 34

Paxton, B., Smolec, R., Schwab, J., et al. 2019, ApJS, 243, 10

Penev, K., Bouma, L. G., Winn, J. N., & Hartman, J. D. 2018, AJ, 155, 165

Pepe, F., Cristiani, S., Rebolo, R., et al. 2021, A&A, 645, A96

Planck Collaboration, Ade, P. A. R., Aghanim, N., et al. 2016, A&A, 594, A13

Rebull, L. M., Stauffer, J. R., Bouvier, J., et al. 2016, AJ, 152, 113

Ricker, G. R., Winn, J. N., Vanderspek, R., et al. 2015, Journal of Astronomical Telescopes, Instruments, and Systems, 1, 014003

Riello, M., De Angeli, F., Evans, D. W., et al. 2021, A&A, 649, A3

Rosenthal, L. J., Fulton, B. J., Hirsch, L. A., et al. 2021, ApJS, 255, 8

Roxburgh, I. W. 2016, A&A, 585, A63

Roxburgh, I. W., & Vorontsov, S. V. 1994, MNRAS, 268, 143

—. 2003, A&A, 411, 215

Samadi, R., Georgobiani, D., Trampedach, R., et al. 2007, A&A, 463, 297

Saunders, N., van Saders, J. L., Lyttle, A. J., et al. 2024, ApJ, 962, 138

Scargle, J. D. 1982, ApJ, 263, 835

Scherrer, P. H., Wilcox, J. M., Christensen-Dalsgaard, J., & Gough, D. O. 1983, SoPh, 82, 75

Seager, S., Knapp, M., Demory, B.-O., et al. 2021, AJ, 161, 117

Sekiguchi, M., & Fukugita, M. 2000, AJ, 120, 1072

Serenelli, A., Johnson, J., Huber, D., et al. 2017, ApJS, 233, 23

Silva Aguirre, V., Davies, G. R., Basu, S., et al. 2015, MNRAS, 452, 2127

Silva Aguirre, V., Lund, M. N., Antia, H. M., et al. 2017, ApJ, 835, 173

Somers, G., & Pinsonneault, M. H. 2015, ApJ, 807, 174

Somers, G., Stauffer, J., Rebull, L., Cody, A. M., & Pinsonneault, M. 2017, ApJ, 850, 134

Sonoi, T., Samadi, R., Belkacem, K., et al. 2015, A&A, 583, A112

Spada, F., Demarque, P., & Kupka, F. 2021, MNRAS, 504, 3128

Spada, F., & Lanzafame, A. C. 2020, A&A, 636, A76

Tanner, J. D., Basu, S., & Demarque, P. 2016, ApJL, 822, L17

Tassoul, M. 1980, ApJS, 43, 469

—. 1990, ApJ, 358, 313

Tayar, J., Claytor, Z. R., Huber, D., & van Saders, J. 2022, ApJ, 927, 31

Teixeira, T. C., Kjeldsen, H., Bedding, T. R., et al. 2009, A&A, 494, 237
Thoul, A. A., Bahcall, J. N., & Loeb, A. 1994, ApJ, 421, 828
Torres, G. 2013, Astronomische Nachrichten, 334, 4
Townsend, R. H. D., & Teitler, S. A. 2013, MNRAS, 435, 3406
Trampedach, R., Asplund, M., Collet, R., Nordlund, Å., & Stein, R. F. 2013, ApJ, 769, 18
Trampedach, R., Stein, R. F., Christensen-Dalsgaard, J., Nordlund, Å., & Asplund, M. 2014, MNRAS, 445, 4366
Ulrich, R. K. 1986, ApJL, 306, L37
van Belle, G. T., & van Belle, G. 2005, PASP, 117, 1263
van Saders, J. L., Ceillier, T., Metcalfe, T. S., et al. 2016, Nature, 529, 181
van Saders, J. L., & Pinsonneault, M. H. 2013, ApJ, 776, 67
Verma, K., Raodeo, K., Basu, S., et al. 2019, MNRAS, 483, 4678
Viani, L. S., Basu, S., Ong J., M. J., Bonaca, A., & Chaplin, W. J. 2018, ApJ, 858, 28
Vidotto, A. A., Lichtenegger, H., Fossati, L., et al. 2018, MNRAS, 481, 5296
Vogt, S. S., Burt, J., Meschiari, S., et al. 2015, ApJ, 814, 12
Weiss, A., & Schlattl, H. 2008, Ap&SS, 316, 99
White, T. R., Bedding, T. R., Stello, D., et al. 2011, ApJ, 743, 161
White, T. R., Bedding, T. R., Gruberbauer, M., et al. 2012, ApJL, 751, L36
White, T. R., Huber, D., Maestro, V., et al. 2013, MNRAS, 433, 1262
White, T. R., Huber, D., Mann, A. W., et al. 2018, MNRAS, 477, 4403
Winn, J. N., Sanchis-Ojeda, R., & Rappaport, S. 2018, NewAR, 83, 37
Wright, J. T. 2018, in Handbook of Exoplanets, ed. H. J. Deeg & J. A. Belmonte, 4
Yu, J., Huber, D., Bedding, T. R., et al. 2018, ApJS, 236, 42
Zhou, J., Bi, S., Yu, J., et al. 2024, ApJS, 271, 17